WAVES AND OSCILLATIONS IN COMPLEX NETWORKS

A Dissertation

Presented to the Faculty of the Graduate School

of Cornell University

in Partial Fulfillment of the Requirements for the Degree of

Doctor of Philosophy

by

Jason Michael Hindes

August 2015

Waves and oscillations in complex networks

Jason Michael Hindes, P.h.D.

Cornell University 2015

Network theory has proven a powerful and general framework for studying the effects of complex interaction topology on the dynamics of many real systems in biology, physics and the social sciences, which show a variety of heterogeneous and multi-scale connectivity patterns. Although much work has been done in this field, many open questions remain about what role network topology plays in influencing the behaviors of complex systems. This dissertation examines the effects of complex network structure on the formation of collective oscillations and waves. In particular we study the propagation of epidemic fronts in multi-scale networks, the interplay between mutual and driven synchronization in heterogeneous oscillator networks, and the emergence of collective transport waves in driven randomly pinned oscillator networks. Qualitatively new behavior is found, and new reduction and analysis techniques are developed which allow us to understand the relationship between connectivity structure and the dynamics in these processes. Broadly, this work makes unique contributions to the exploration of fully non-equilibrium pattern formation and nonlinear dynamics in complex networks.

BIOGRAPHICAL SKETCH

Jason Michael Hindes was born on December 19, 1987, into a family of two great parents, with two great brothers, in Port Huron Michigan, where the Saint Clair and Black rivers flow into the Great Lakes.

From a young age he was eager, precocious, and aspired to everything. Though he was quiet, he had an appetite for discovery and exploration. The latter impelled him to not a few devious acts before the age of five – Galileo had cannonballs and the Tower of Pisa; Jason had household treasures and a rooftop.

Perhaps because of this (or despite it) he performed very well in school, winning plenty of spelling bees and math flashcard competitions – unfortunately the former talent seems to have left him. Over the years, however, academic success came too easy (in the early days), and did not engage his intellect. For that he had his guitar: his first love.

From age ten until seventeen, Jason focused nearly all of his effort and attention on playing the guitar – punctuated from time to time by a similar obsession with soccer. Mornings before school, he would wake up at 5:00 am so that he could practice his modes and scales, repeating chromatic movements on every string and fret. The discipline was only half of the love, the other half was creativity – a beautiful thing. Once he had mastered the techniques, an infinite space of music could be engineered – carefully, sturdily; structures with prodigious complexity or sharp simplicity. And so, he started to write.

It was probably this which seeded his intellectual style. The approach was to listen to as much strange and beautiful music as possible and pay attention to what the writers were trying to do, or what new approaches they were trying to introduce. Was there anything general and serviceable in the music, that could help Jason work through the barriers in his own creative work?

Somewhere around the same time (perhaps at age 15), Jason came across a book, titled “The

Elegant Universe", by Brian Greene, and it started another love story. Though the concepts in it were harder to grasp and more esoteric than music, he was overwhelmed with the scope and breadth of physics – its universality, the power of ideas expressed in mathematics over the world,... hit him like a lightning stroke (it still does). Here again was an opportunity to master, create, and explore. Not only that, but once learned, there was a promise of "explaining the world." From that moment he devoured science writing, in and outside of the classroom walls. Amazingly, his school helped him indulge this craving, and let him skip the normal physics classes, and conduct an independent study in the subject, which eventually led him to winning the high-school science award.

Jason took his love for science to the University of Michigan, where he majored in physics and performed research in experimental particle physics (culminating in a four month REU at CERN and an undergraduate thesis that won the department's highest award – though, seeing Lake Léman rest beneath Mt. Blanc was way better than any prize). Despite his affection for fundamental physics that began with reading Greene's book, over time he started to wonder if the field was loosing its groove: the experiments were so big and took so long to build, and the theories seemed to have less and less connection to the world. Around this depressing time, Jason took a class with Mark Newman, the leading expert on the statistical mechanics of complex networks, fell in love with the subject of physics again, and accepted an offer to attend Cornell University for graduate studies, circa 2010.

The rest of the story is the content of this thesis.

DEDICATIONS

Not only for this work, but for everything that I ever have or will accomplish, I thank: my parents, Michael and Kathy Hindes, for their grace and leniency, and for teaching me how to love, my grandparents, Donald and Valery Hindes and Emil and Elaine Barthel, for their probity and steadfastness, and for their cheers in every crowd and soccer game, my brothers Nick Hindes and Wade Hindes, for their wit and intelligence, and for all the laughs and all the moments when hands fall down on shoulders, my wife Erin Almand Hindes, for her cloudless love shining down on all places, and for her patience when mine has long since evaporated, and our " pups", Moose and Piper, for dragging me away from my work with panting tongues and wet noses, and making me see the real world... This is, and always will be, for you.

ACKNOWLEDGMENTS

First, I would like to thank my adviser, Chris Myers, for his friendship and patience in working with me. I have enjoyed our time together immensely, and am deeply grateful for his support.

Second, I would like to thank my adviser-part-two, Dave Schneider, for his friendship and guidance, and for taking the chalk out of my hands from time to time.

I sincerely thank Jim Sethna and Carl Franck for serving on my special committee.

I thank my friends Lei Huang, Sarabjeet Singh, Oleg Kogan, Drew Dolgert, Eli Bogart, and Daniel Citron for their insights, wisdom, banter, and philosophical discussions that rambled on for too long.

I thank John Guckenheimer for interesting conversations on nonlinear dynamics, where he is the king.

This work was supported by the Science and Technology Directorate of the U.S. Department of Homeland Security via the interagency agreement no. HSHQDC-10-X-00138, and a Cornell University Graduate Student Fellowship (2010-2011).

TABLE OF CONTENTS

Part I

INTRODUCTION

It is a bit treacherous to look back at the past and try to foist a simple narrative on it. Probably my own course in physics research was set by a complicated jumble of historical accidents, aesthetic prejudices, and tactical judgments about what problems are worth thinking about. Nevertheless, some salient features and ideas do seem to appear, and it is my purpose here to put them in plain view. This, I hope, will better orient the reader in navigating the pages that follow.

To start, I should say that one of my deepest interests is in emergent phenomena – that tendency for large systems of interacting things to produce collective behavior that is interesting in ways that individual things are not [81]. Not only are such phenomena fascinating in themselves (one can't help thinking about flocking birds), but as a physicist, one wonders if there are principles underlying them, and if so, how do they arise [82]?

But, where to start? This is when tact makes its appearance. As a theorist, the approach is generally two-fold once one has settled on an interesting phenomenon. First, one writes down a simple model. We justify this in various ways: "You don't need something more, to get something more" as Murray Gell-Mann would put it, is a typical refrain. Certainly a major virtue of studying simple models is that they offer a chance (if one is lucky) of making tight deductions, i.e., "*this* model produces *this* behavior", which makes it easier to really feel like you understand something, and helps you sleep at night. Another argument gestures in the direction of renormalization, which for deep reasons, makes us think that collective effects are determined by general features of a problem [17]. And so, cooking up more and more complicated models, often doesn't add anything, except perhaps, confusion. The second step in the approach, is to focus on points where collective behaviors "break," or change their form when you "poke" the system. Often, we find that by understanding how different regions of behaviors are fused at

"phase transitions", we find the seeds of everything else that we observe [17, 83].

This form is standard in my own subfield, where one explores the role of complex network topology, that specifies the patterns of interaction in a system, in determining its behavior [2, 42, 44]. As a consequence of this focus on networks, throughout these pages, you will see an emphasis on certain topological features in a given problem, with less detailed descriptions of the interaction principles themselves, which have been motivated in many other works. There are two main components that make up my interest in networks. The first is that many real systems have been shown to interact through complex networks, extensively catalogued across the sciences (some of which are discussed here), with patterns of connection that do not find counterparts in solid-state physics [42]. This fact forces us to grapple with complex networks if we want to extend our physics beyond the typical states of matter. The second is that network theory, because of its formulation in terms of topology, offers a very general way of doing statistical physics, and therefore may offer an avenue for deepening the principles of statistical physics. A small example network is shown in Fig.1 that demonstrates the basic construction, which will be standard throughout this thesis.

Probably, the scientific interest in complex networks began with the work of Watts and Strogatz, who were studying models of synchronization for fireflies, and noticed that when one adds a few random links to a regular interaction network, like a lattice, the resulting network is "small world" (the average distance between nodes is small) and keeps its finite clustering (the fraction of neighbors who share neighbors is large)[84]. This balance between randomness and clustering, greatly improves the synchronizability of coupled oscillator networks, and was found in many real world examples (including the neural network of C. elegans and the U.S. power grid). Building on these insights many started to measure the properties of real-world networks by collecting a wealth of data in a vast number of disciplines and noticed ubiquitous, complex features including: power-law degree distributions (the fraction of nodes that have some number of neighbors follows a power law; e.g., the world-wide-web), fractal structure (Russian

doll form, which most often occurs in biology; e.g., gene regulatory networks), modularity (networks built of several densely connected communities; e.g., neural networks), and multi-layer (networks have many overlapping types of interactions simultaneously) [4, 86–88]. This lead to an explosion of theoretical studies on ways of producing networks with the above properties as well as others, and studies of network behavior, given these properties, in various dynamical processes [43, 44, 89]. This is where our work begins.

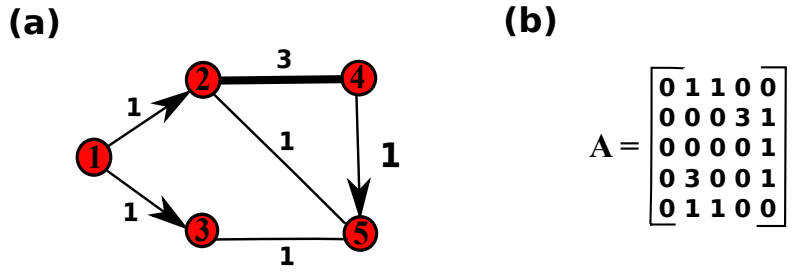

Figure 1: (a) A network (or graph) consisting of five nodes (red circles) and six edges (black lines). Typically, the nodes represent agents and the edges represent some interaction between them. Nodes are labeled with integers, 1...5, and edges are labeled according to their weight (note: all edges have weight equal to one except for the top edge which has weight equal to three). Arrows indicate when an edge points in a single direction. Edges without arrows are bidirectional. (b) The adjacency matrix representation, A, for this network where the i, j element specifies the weight of the edge from node i to node j; if no edge exists, then the matrix element is zero (note: if there is a directed edge from j to i, but not from i to j, the matrix element is zero).

Though the study of complex networks is a very large industry, non-equilibrium phenomena and phase-transitions in such systems are to a great extent frontiers, particularly in areas involving pattern formation and non-linear dynamics. Dealing explicitly with the dynamics of networks is hard for many reasons, not least of which is because it is often expressed in high-dimensional equations. Perhaps because of this, the majority of results to date have centered around the structure of networks or on their equilibrium behaviors such as percolation properties and steady states of epidemic models [2, 42, 44]. Even non-equilibrium behaviors, such as the

mutual synchronization of coupled oscillators or the finite-size fluctuations in endemic stochastic processes on networks, can be studied in a very similar way [90–92]. But what happens if we are interested in something transient, such as the propagation of disease through interconnected networks, or we are interested in a network whose dynamics is excited by external forces, and the behavior is inherently not in equilibrium? This is where I have pointed my telescope, and some of what I found is before the reader.

Beyond my interest in dynamics, my selection of problems has three underlying criteria that the reader may notice. The first is that the phenomena studied should be important and general – showing up in many different applications. This is certainly the case for self-limiting reaction fronts (such as the spread of disease) and collective waves and oscillations in coupled nonlinear oscillators, both of which are discussed in detail in the following. The second is that network structure should cause *new* behavior, which is not observed in simpler systems. The third is that the introduction of network structure should motivate the development and generalization of techniques from statistical physics to the strange land of complex systems. You will find some of all three in this work.

One last point for the initiated reader. Most of the networks that we treat in our models are random graphs with some specified quantities, e.g., a degree distribution [1, 26]. This construction is useful for several reasons: it allows us to understand how the dynamics we are studying changes as a function of local network properties, and we find that these constructions are the simplest way to "kick" the behavior out of the all-to-all or mean-field universality classes, which are usually known, into new ones [72]. Nevertheless, in several places we offer thoughts on more general types of structure and techniques which will be explored in future work.

Part II

EPIDEMIC FRONTS IN COMPLEX NETWORKS WITH METAPOPULATION STRUCTURE

Summary: Infection dynamics have been studied extensively on complex networks, yielding insight into the effects of heterogeneity in contact patterns on disease spread. Somewhat separately, metapopulations have provided a paradigm for modeling systems with spatially extended and "patchy" organization. In this work, we expand on the use of multitype networks for combining these paradigms, such that simple contagion models can include complexity in the agent interactions and multiscale structure. We first present a mean-field approximation for Susceptible-Infected-Recovered (SIR) dynamics on multitype networks. We then use this technique to study the case of epidemic fronts propagating on a one-dimensional lattice of interconnected networks – representing a simple chain of coupled population centers – as a first step in understanding how macro-scale disease spread depends on micro-scale topology. Using the formalism of front propagation into unstable states, we derive the emergent transport coefficients of the epidemic spreading: asymptotic speed, characteristic wavelength, and diffusion coefficient for the leading edge of the pulled fronts, and analyze their dependence on the underlying graph structure. We also derive the epidemic threshold for the system and study the front profile for various network configurations. We find that networks with large fluctuations and correlations in their contact structure produce very fast fronts with broad profiles, suggesting a separation of time-scales between propagation and the epidemic. To our knowledge, this is the first such application of front propagation concepts to random network models [1].

[1] The material in Part II is reproduced from [70]

I. Introduction

Network theory is a very useful framework for studying the effects of randomness and heterogeneity on the dynamics of interacting agents with non-trivial connectivity patterns [1]. One of the most important applications of this work is to the spread of infectious diseases among human populations, where the interaction structure is highly complex, showing salient features such as power-law degree distributions, small average path lengths, and modularity [2, 44]. Various models have been proposed, primarily with random graph configuration, that incorporate these complex features while remaining theoretically tractable. Within the context of disease dynamics, graph nodes are generally taken to represent individuals, and edges to represent interactions between them, through which infection can spread. Both deterministic and stochastic infection dynamics have been studied on networks as well as bond percolation for the associated branching process [5, 6, 10, 11, 13]. How various thermodynamic quantities of interest – such as the steady state incidence, the epidemic (percolation) threshold, and the distribution of small outbreak sizes – depend upon network topology is of great interest.

However, often these approaches disregard the multiscale organization of many real systems, in which agents can be most naturally thought of as partitioned into densely connected communities with sparser coupling among neighboring communities. In some cases, it may be useful to conceptualize the topology as a network of networks, where agent-to-agent interactions and community-to-community interactions are both useful representations depending on the scale of resolution [8]. The latter has been successfully developed in ecology, with a network of interconnected populations referred to as a "metapopulation" [18, 19]. This framework is very useful in studying large scale propagation of diseases where most infection transmission occurs in localized regions, but can be transported on larger scales by the mobility of individuals, traveling among population centers [30]. However, most metapopulation models assume that populations are fully mixed, with no inherent complexity in the connectivity between agents.

Much less understood is how the multiscale structure of agent interactions affects the larger scale propagation of infectious processes through interconnected networks [25, 27].

In the following sections, we expand on a possible avenue for addressing these questions using a multitype generalization of random graphs with simple, meta-level topology [8, 9], and construct a dynamical mean-field theory for the SIR infection model in multitype configuration model networks. Putting these together, we analyze the average infection dynamics and propagating front profile on a simple metapopulation composed of coupled population centers on a one-dimensional lattice and calculate the phenomenological transport properties of the system as functions of the underlying network's degree distributions. Our results are compared to stochastic simulations of the infection kinetics on various networks and found to be in good agreement in the thermodynamic limit. Broadly, we present this work as an illustration of how well-developed ideas from different areas of statistical physics and ecology can be naturally combined.

II. Multitype Configuration Model Networks

In order to incorporate relevant node attribute information into our network models, (generically applicable for such things as age, sex, ethnicity, and place of residence), we use a generalization of configuration model random graphs, wherein nodes are assigned a type from an arbitrary set of M possible types and a degree to each type from an arbitrary joint distribution for degree types, $P_i(k_1, k_2, ...k_M) = P_i(\vec{k})$, with degree k_j denoting the number of connections to nodes of type j [1, 8, 9, 12]. Additionally, nodes of type i occupy a fraction of the total network w_i, where $\sum_i w_i = 1$. Following the configuration model prescription, we consider graphs chosen uniformly at random from the ensemble of possible graphs with the prescribed degree distributions and self-consistent edge constraint: $w_i \sum_{\vec{k}} k_j P_i(\vec{k}) = w_j \sum_{\vec{k'}} k'_i P_j(\vec{k'}), \forall (i,j)$[1, 4, 9].

From this formalism, a variety of quantities can be described compactly using generating functions [1, 7]. For instance, the generating function for the probability of a randomly selected

node of type i to have degree $\vec{k}$, is given by

$$G_i(\vec{x}) = \sum_{\vec{k}} P_i(\vec{k}) \prod_{l=1}^{M} x_l^{k_l} : \tag{1}$$

written as a power series in $\vec{x}$, an auxiliary variable defined over the unit interval, with expansion coefficients equal to the respective probabilities. Moments of the degree distributions can be represented simply as derivatives of the corresponding generating function. For example, the average degree of a type i node to a type j node is

$$\sum_{\vec{k}} k_j P_i(\vec{k}) = \partial_{x_j} G_i(\vec{x})|_{\vec{1}} \equiv \langle k_j \rangle_i \,. \tag{2}$$

Since node interactions occur along edges, an important quantity in network models is the excess degree: the number of neighbors a node has which can be reached by selecting a randomly chosen edge, and not including the neighbor on the end of the selected edge. For a multiype configuration model network, the probability that a randomly chosen edge from a type i node leads to a type j node with degree $\vec{k}$ is proportional to $k_i P_j(\vec{k})$, and thus the probability for the corresponding excess degree is generated by $\partial_{x_i} G_j(\vec{x}) / \partial_{x_i} G_j(\vec{x})|_{\vec{1}}$ [9], with average degree to type l nodes,

$$\langle k_l \rangle_{i-j} = \frac{\partial_{x_l} \partial_{x_i} G_j(\vec{x})|_{\vec{1}}}{\partial_{x_i} G_j(\vec{x})|_{\vec{1}}} = \frac{\langle k_l k_i \rangle_j}{\langle k_i \rangle_j} - \delta_{il}. \tag{3}$$

By construction, this framework lacks two-point correlations, in which the excess degree distributions depend on the degrees of both nodes sharing an edge [44].

III. Mean-Field SIR in Multitype Networks

In this work we consider simple dynamics for disease spread: the Susceptible-Infected-Recovered (SIR) model, wherein each individual is assigned a disease state, $Y \in \{S, I, R\}$,

and may undergo stochastic reactions to other states depending on its state and the state of its neighbors. In this model, if a node of type i is susceptible and has a single infected neighbor of type j, then it will change its state to infected with a constant probability per unit time β_{ji}. Likewise, an infected node of type i will recover with a constant probability per unit time γ_i. Since the underlying dynamics is constructed to be a continuous time Markov process, a complete analysis would describe the full probability distribution for all system trajectories. However for our purposes, it will be sufficient to focus on the behavior of extensive outbreaks (i.e., those which scale with the system size), the average dynamics of which, can be derived in the limit when the number of nodes tends to infinity, by generalizing a mean-field technique for single type networks, developed by Volz and Miller, to multitype networks. Below, we follow the basic structure of the derivations presented in [14, 15].

In the thermodynamic limit, configuration model random graphs are locally tree-like [4], which by construction allows them to satisfy many of the generic criteria for the applicability of mean-field theory assumptions [16]. In our case, we assume that nodes are differentiated by their degree and disease state alone and that susceptible nodes feel a uniform force of infection along every edge, related to the average number of edges connecting susceptible and infected nodes at any given time in the network: a Curie-Weiss type approximation [17]. Furthermore, from the perspective of susceptible nodes, all infection attempts along different edges can be treated as uncorrelated – a consequence of the local tree-like property [4, 6, 14]– and thus we assume that the states of neighbors of susceptible nodes are effectively independent.

Let the probability that a node of type j has not transmitted the infection to a node of type i along a randomly chosen $i-j$ edge, be θ_{ij}. This quantity is interpretable as the complement of the average cumulative hazard function along such edges. Given θ_{ij}, it follows that the fraction

of susceptible nodes of type i at time t is

$$S_i(t) = \sum_{\vec{k}} P_i(\vec{k}) \prod_{j=1}^{M} \theta_{ij}^{k_j}(t) = G_i(\theta_{i1}(t), \theta_{i2}(t), ...\theta_{iM}(t))$$
$$\equiv G_i(\vec{\theta}_i(t)). \tag{4}$$

The fractions of infected and recovered nodes of type i follow from probability conservation, $S_i + I_i + R_i = 1$, and a constant recovery rate for infected nodes γ_i:

$$\frac{dI_i}{dt} = -\frac{d\vec{\theta_i}}{dt} \cdot \vec{\nabla} G_i(\vec{x})|_{\vec{\theta}_i} - \gamma_i I_i$$
$$\frac{dR_i}{dt} = \gamma_i I_i \ , \tag{5}$$

with the total fraction of susceptible nodes

$$S = \sum_i w_i G_i(\vec{\theta}_i) \equiv \vec{w} \cdot \vec{G}(\underline{\theta}). \tag{6}$$

The central probability and order parameter, θ_{ij}, can be subdivided into three compartments depending on the disease state of the terminal node j,

$$\theta_{ij} = \theta_{ij}^S + \theta_{ij}^I + \theta_{ij}^R \ , \tag{7}$$

and its dynamics determined by tracking the fluxes among these compartments. Since θ can only change when an infected node transmits the disease, the rate at which θ_{ij} changes is equal to the rate at which a corresponding neighbor infects, and therefore $d\theta_{ij} = -\beta_{ji}\theta_{ij}^I dt$. Similarly, since θ^R can only change if an infected node recovers, the rate at which θ_{ij}^R changes is equal to the rate at which a corresponding neighbor recovers, and thus $d\theta_{ij}^R = \gamma_j \theta_{ij}^I dt$. Lastly, the probability that a type j neighbor of a type i node has not transmitted and is susceptible, θ_{ij}^S, is simply the probability that the corresponding neighbor is susceptible. Because this neighbor

could not have been infected along any of its other edges and has excess degree distribution generated by $\partial_{x_i} G_j(\vec{x})/\partial_{x_i} G_j(\vec{x})|_{\vec{1}}$, it follows that $\theta_{ij}^S = \partial_{x_i} G_j(\vec{x})|_{\vec{\theta}_j}/\partial_{x_i} G_j(\vec{x})|_{\vec{1}}$. Combining the latter with the two flux relations and the initial conditions (7), $\theta_{ij}(0) = 1$ and $\theta_{ij}^R(0) = 0$, we find

$$\frac{d\theta_{ij}}{dt} = \beta_{ji}\left(\frac{\partial_{x_i} G_j(\vec{x})|_{\vec{\theta}_j}}{\partial_{x_i} G_j(\vec{x})|_{\vec{1}}} - \theta_{ij}\right) + \gamma_j\left(1 - \theta_{ij}\right). \tag{8}$$

These M^2, first-order and coupled ODEs, $\dot{\underline{\theta}} = \underline{\underline{F}}(\underline{\theta})$, define the full system's approximate mean dynamics, and form the basis of our analysis below.

The steady state is given by the fixed point of (8),

$$\bar{\theta}_{ij} = (1 - T_{ji}) + T_{ji}\frac{\partial_{x_i} G_j(\vec{x})|_{\vec{\bar{\theta}}_j}}{\partial_{x_i} G_j(\vec{x})|_{\vec{1}}}\ , \tag{9}$$

which upon substitution into (4), gives the cumulative infection, $P = 1 - S$, at equilibrium (i.e., the final epidemic size), with $T_{ji} = \beta_{ji}/\left(\beta_{ji} + \gamma_j\right)$ the corresponding bond percolation probability, or transmissibility [9]. This can have a non-trivial solution corresponding to the existence of extensive outbreaks, if the disease-free state, $\theta_{ij} = 1 \quad \forall(i,j)$, is unstable. The threshold or phase transition, which signifies the region in parameter space that separates the epidemic and non-epidemic phases, can be obtained through a stability analysis of the disease-free state, where the eigenvalue of the Jacobian for (8) with the largest real part, is real and

vanishes when

$$det(\underline{\underline{R}} - \underline{\underline{I}}) = 0, \quad \text{with} \tag{10}$$

$$R_{(i,j)(k,l)} = T_{ji}\delta_{jk}\left\langle k_l \right\rangle_{i-j}$$

an M^2xM^2 matrix [33], giving a generalization of the basic reproductive number of a disease R_0, that incorporates the varying degrees of local connectivity. Similar results for the equilibrium properties are derivable from a multitype bond percolation approach [9].

IV. Framework for Multiscale Networks

Of interest to us are systems where type structure adds an additional scale of relevant topology, and not just demographic complexity [8, 9]. For instance, we can apply the multitype network formalism to a simple model for a metapopulation by affiliating population centers with node types and coupling among populations with edges connecting their constituent nodes. In this way, a complex topology can be encoded on a micro-scale with a macro-scale adjacency matrix, $\underline{\underline{A}}$, describing which populations are directly connected through node interactions [8]. As a simple but useful example implementation, one could first specify an $\underline{\underline{A}}$ of interest that distinguishes whether or not interactions can occur between neighboring populations (e.g., $A_{i,j} = 1$ if i and j interact and zero otherwise – perhaps derived from a transport network), and then connect nodes among the connected populations with some local edge-distribution of interest (see Sec.V)[2]. We envisage example systems where $\underline{\underline{A}}$ describes the connectivity among urban centers, such as cities, towns, or villages, facilitated by roads or airlines. By conceptualizing the topology in this manner, we can study the phenomenology of infection propagation among population centers and describe how the emergent propagation properties depend on the underlying

[2] If one knows the full probability distribution for degrees and types (populations), the adjacency matrix for the populations is redundant. However, the construction we mention is useful if the latter is known, with less known about the exact distribution of micro-scale connections.

connectivity patterns. A schematic is shown in Fig.2-(a) for a simple system with the pertinent structure. More broadly, we advance this approach as an avenue for combining the frameworks of network theory, metapopulations, and front propagation, which will be particularly useful if the interaction topology is coherent after some level of coarse graining.

V. 1-d Lattice Metapopulation Dynamics

To illustrate this approach, we consider a special case of the above where the macro-scale topology is an infinite one-dimensional lattice, $M \to \infty$, in which agents interact with other agents of the same type and agents of neighboring types, $A_{nj} = (\delta_{j,n} + \delta_{j,n+1} + \delta_{j,n-1})$ (applicable to simple commuter schemes [30]). If infection is started at a single site (e.g., site 0) in a fully susceptible system, a strict directionality applies: in order for site i to be infected, sites $i-1, i-2, ...$ must be infected first. In such a case, we expect a well-defined infection front to propagate through the lattice. In keeping with the above, we focus on an effective force of infection model among populations with static configuration networks having prescribed degree distributions – a generalization of the paradigmatic, spatial SIR model in one dimension, where the assumption of well mixed populations is relaxed to include complexity in agent interactions [19, 20]. A schematic is shown in Fig.2-(b).

Since each node has three edge types, the mean equations of motion describe a three-component field, $\vec{\theta}_n(t) \equiv (\theta_{nn}, \theta_{nn+1}, \theta_{nn-1}) \equiv \left(\theta_n^0(t), \theta_n^+(t), \theta_n^-(t)\right)$, where (0), (+), and (−) denote internal, right-external, and left-external edges, at the corresponding site. For simplicity, homogeneity is assumed, with β, w, γ, and G all uniform – reducing the field equations to

$$\begin{aligned} \frac{d\theta_n^0}{d\tau} &= (1-\theta_n^0) + T\left(\frac{G_0(\vec{\theta}_n)}{G_0(\vec{1})} - 1\right), \\ \frac{d\theta_n^\pm}{d\tau} &= (1-\theta_n^\pm) + T\left(\frac{G_\mp(\vec{\theta}_{n\pm1})}{G_\mp(\vec{1})} - 1\right), \end{aligned} \tag{11}$$

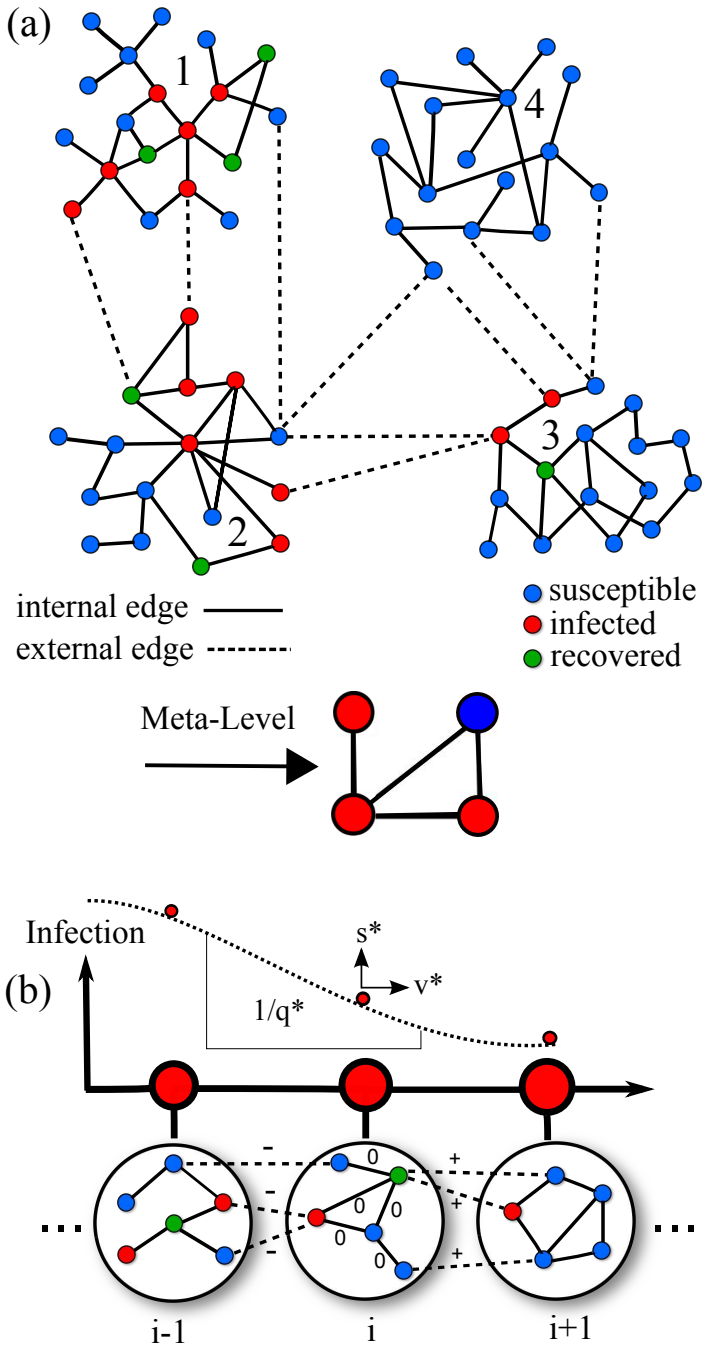

Figure 2: (a) A schematic of SIR dynamics on a metapopulation, where infection spreads along edges connecting nodes of various types at the finest scale (shown with integer, population labels), and the macro-scale topology identifies which populations are directly connected through agent interactions. (b) A particular example of this framework, in which the macro-scale topology takes the form of a one-dimensional lattice. In Sec.V, we focus on a simple case with configuration model construction, where each site has an identical degree distribution, specifying the probability of having a given number of internal (0), right (+), and left (-) external edges (shown above with labels for site i).

where the time, τ, is measured in units of $1/(\beta+\gamma)$, and the subscript in G denotes a partial derivative with respect to the corresponding variable. For edge number consistency, $G_+(\vec{1}) = G_-(\vec{1})$, but in general we allow for other asymmetries in the degree distributions.

A. Dispersion Relation and Transport Coefficients

To understand the spatio-temporal dynamics (11), we first quantify how perturbations away from the unstable state propagate in space by linearizing the dynamics around the disease-free equilibrium, $\vec{\theta}_n(t) = \vec{1} - \vec{\epsilon}_n(t)$, and decoupling the perturbations into basis modes using the Inverse Discrete Fourier Transform, $\vec{\epsilon}_n(t) = \frac{1}{M}\sum_{\nu=0}^{M-1} \vec{\epsilon}_\nu(t) e^{i(2\pi\nu n/M)}$, (IDFT). The dispersion relation can be found by substituting the IDFT into (11) and using the basis properties of orthogonality and completeness. In the limit $M \to \infty$, the site perturbations approach an integral in a continuous wave vector: $k \equiv \frac{2\pi\nu}{M}$, $\vec{\epsilon}_n(t) = \frac{1}{2\pi}\int_0^{2\pi} \vec{\epsilon}(k) e^{i(kn-\omega(k)t)} dk$.

With this prescription, we find the dispersion relation takes the form of a cubic, characteristic equation

$$\det\left(\underline{\underline{K_e}}(q) - \frac{1+s(q)}{T}\underline{\underline{I}}\right) = 0, \qquad \text{with} \tag{12}$$

$$\underline{\underline{K_e}}(q) = \begin{bmatrix} \frac{\langle k_0^2\rangle}{\langle k_0\rangle} - 1 & \frac{\langle k_0 k_+\rangle}{\langle k_0\rangle} & \frac{\langle k_0 k_-\rangle}{\langle k_0\rangle} \\ \frac{\langle k_- k_0\rangle}{\langle k_-\rangle} e^{-q} & \frac{\langle k_- k_+\rangle}{\langle k_-\rangle} e^{-q} & \left(\frac{\langle k_-^2\rangle}{\langle k_-\rangle} - 1\right) e^{-q} \\ \frac{\langle k_+ k_0\rangle}{\langle k_+\rangle} e^{q} & \left(\frac{\langle k_+^2\rangle}{\langle k_+\rangle} - 1\right) e^{q} & \frac{\langle k_+ k_-\rangle}{\langle k_+\rangle} e^{q} \end{bmatrix}$$

which for convenience, is written in terms of s and q – the rate and wave number of the epidemic – where $\omega = is$ and $k = iq$. Interestingly, this method reveals a generalization of the average excess degree matrix, $\underline{\underline{K_e}}(0)$ – whose elements are found by selecting a randomly chosen edge in a particular direction, and counting the average number of reachable neighbors of a particular type – for the interconnected network system, $\underline{\underline{K_e}}(q)$, which incorporates the relative states of

adjacent sites on the lattice for each q-mode. We expect this operator to emerge in similar front propagation problems on interconnected networks.

Combining the above with the behavior of infection near the phase transition, where there is no exponential growth in time and each site has the same field value: $s \to 0$ and $q \to 0$ (12), we find a simple condition for the critical transmissibility T_c:

$$T_c = \frac{1}{\lambda_m^k(0)} \ , \tag{13}$$

where $\lambda_m^k(q)$ is the maximum eigenvalue of $\underline{\underline{K_e}}(q)$, with $\lambda_m^k(0)$ corresponding to $\underline{\underline{K_e}}(0)$. Because the addition of external edges increases the spreading capacity of the disease, the critical transmissibility in the coupled system is less than the uncoupled case, implying that transport-mediated infections from neighboring sites can sustain epidemics even when individual populations on their own cannot [25, 27].

Also from the dispersion relation, we can find the asymptotic transport coefficients for rightward moving disturbances by making a standard saddle-point approximation of the perturbations' integral representation in Fourier space: expanding the integrand around its dominant contribution, k^*, in the co-moving frame, $\xi = n - v^* t$,

$$e^{i(kn-\omega(k)t)} \sim e^{ik\xi} e^{it\left(kv^*-\omega(k^*)-\frac{d\omega}{dk}\Big|_{k^*}(k-k^*)\right)} e^{\frac{-it(k-k^*)^2}{2}\frac{d^2\omega}{dk^2}\Big|_{k^*}}$$

and taking the infinite time limit while enforcing approximate constancy with no exponential growth of the field[3] and ξ finite – where v^* is the asymptotic speed at which perturbations to the unstable state propagate [22]. This procedure uncovers an exponential moving pulse for the

[3] in the co-moving frame.

leading-edge of the infection profile with a diffusive correction [22] [4]:

$$1-\theta \sim \frac{e^{-q^*\xi}e^{-\xi^2/4D^*t}}{\sqrt{D^*t}}\ , \tag{14}$$

where q^*, v^*, and D^* satisfy the saddle-point relations:

$$v^* = \left.\frac{ds}{dq}\right|_{q^*} = \frac{s(q^*)}{q^*} = T\left.\frac{d\lambda_m^k}{dq}\right|_{q^*} = \frac{-1+T\lambda_m^k(q^*)}{q^*} \tag{15}$$

$$\text{and} \quad D^* = \frac{1}{2}\left.\frac{d^2s}{dq^2}\right|_{q^*} = \frac{T}{2}\left.\frac{d^2\lambda_m^k}{dq^2}\right|_{q^*}\ , \tag{16}$$

giving a transcendental equation for q^*. When the average excess degree matrix is irreducible (the domain of interest to us), the dominant growth exponent for each q is real and corresponds to a uniquely positive eigenvector (12) [33], and thus we expect the same selected velocity for all fields [24]. Approximately, the fields propagate in this regime with proportions $\vec{1}-\epsilon(t)\vec{Q}(q^*,s^*)$, where $\vec{Q}(q^*,s^*)$ is the corresponding mode of $\underline{\underline{K_e}}(q^*)(12)$. If multiple solutions exist for v^*, the fastest solution is selected [22]. The characteristic wavelength, $1/q^*$, is related to the asymptotic size of the front's leading edge, and diverges near the phase transition. The diffusion coefficient, D^*, gives the effective widening of the mean-field pulse in the co-moving frame and is proportional to the largest finite-size correction to v^* in the limit where the number of nodes at each site tends to infinity.

In order to uncover the principal dependencies of the transport coefficients, we study (12)-(16) near the phase transition, where the power series expansion for the dispersion relation is a convenient representation; the latter is found by substituting $(s(q)+1)/T = a+bq+\frac{c}{2}q^2+...$ into (12), and equating powers in q. When s^* and q^* are small in the vicinity of T_c, the expansion

[4] Eq.(14) is a version of the standard formula for the saddle-point approximation of an integral.

can be truncated at low order, giving a Fisher-Kolmogorov-like dispersion relation with the approximate scaling

$$s^* \sim \left(T\lambda_m^k(0) - 1\right) \qquad v^* \sim \left(T\lambda_m^k(0) - 1\right)^{\frac{1}{2}} {D^*}^{\frac{1}{2}}$$
$$q^* \sim \left(T\lambda_m^k(0) - 1\right)^{\frac{1}{2}} {D^*}^{-\frac{1}{2}} \qquad \frac{D^*}{T\lambda_m^k(0)} \sim \delta$$

$$\delta = \frac{\frac{\langle k_- k_0\rangle\langle k_0 k_+\rangle}{\langle k_-\rangle\langle k_0\rangle} + \frac{\langle k_- k_+\rangle}{\langle k_-\rangle}\left(\lambda_m^k(0) - \frac{\langle k_0^2\rangle}{\langle k_0\rangle} + 1\right)}{\left(\lambda_m^k(0) - \lambda_2^k(0)\right)\left(\lambda_m^k(0) - \lambda_3^k(0)\right)}\,, \tag{17}$$

where $\lambda_2^k(0)$ and $\lambda_3^k(0)$ are the subdominant eigenvalues of $\underline{\underline{K_e}}(0)$. In this regime, we find an effective reaction-diffusion behavior with the generic dependence of the shape and speed of the propagating front's leading edge on the reproductive number $T\lambda_m^k(0)$ (a product of the spreading capacity along edges and the magnitude of topological fluctuations) and on the normalized diffusion coefficient δ: measuring the relative strength of connection between lattice sites (17). We see that the effective reaction rate is equal to the distance from the phase transition, $T\lambda_m^k(0) - 1$, and that all coefficients grow from zero with this distance, except for D^* which varies discontinuously through T_c. Furthermore, the normalized diffusion coefficient increases from zero with $\langle k_- k_0\rangle \langle k_0 k_+\rangle$ and $\langle k_- k_+\rangle$ – the correlation moments of the degree distribution which encode the propensity for transport from the $i \mp 1$ site to the $i \pm 1$ site (both of which cannot be zero, otherwise epidemics are locally confined), and with the viability of subdominant modes to support growth. Generically, we find that as δ increases: v^* and D^* increase, q^* decreases, and s^* remains constant, implying faster transport and greater similarity among sites, as more edge-type pairs allow for traversing the lattice, but with little change in the growth exponent.

The above demonstrates the typical trend for such models, that the front dynamics is strongly influenced by the joint degree distribution's second moments (i.e., the relevant excess degree

properties are generally amplified by fluctuations and correlations among degree types). For example, in analogy with the single network case, very fast transport can be achieved with the presence of a small fraction of nodes with large internal and external degrees, or "transport hubs", even if the average degrees in the network are order one [2, 44].

B. Simple Mixing Example

Additional understanding of the basic form of the transport coefficients is gained by looking at a special case of the micro-scale degree distribution, where the generating function takes the form $G\left(fx_0 + \frac{1-f}{2}(x_+ + x_-)\right)$, with total degree described by G, and a given edge connecting nodes of the same site with probability f, and nodes of left and right neighboring sites with equal probability $(1-f)/2$, where $1-f$ is an effective mixing parameter among populations. With this prescription, the critical transmissibility is reduced to the inverse of the total-edge excess degree, $T_c = \frac{G'(1)}{G''(1)}$, and the normalized diffusion coefficient, to the fraction of external edges in a each direction, $\delta = (1-f)/2$. Moreover, the dispersion relation takes the instructive form

$$s(q) = -1 + \frac{TG''(1)}{G'(1)}\left(f + (1-f)\cosh(q)\right) \ , \tag{18}$$

where $s+1$ is given by the basic reproductive number multiplied by the average relative incidence, $e^{-\Delta nq}$, on the end of a randomly selected edge – illustrating the intuitive generalization of the single network case, where different edge types are more and less likely to connect to infected nodes depending on their place in the lattice, and thus to contribute to local growth.

Likewise, from (15) and (16), we find the speed and diffusion coefficient,

$$v^* = \frac{TG''(1)}{G'(1)}(1-f)\sinh(q^*) \tag{19}$$

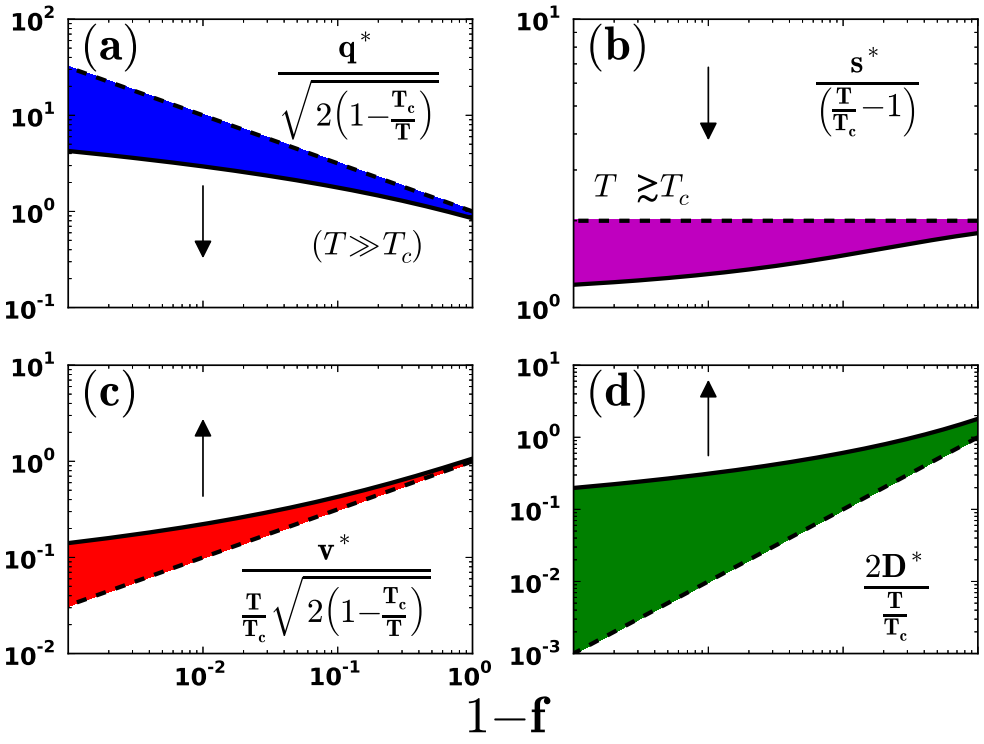

Figure 3: The scaled transport coefficients for a one-dimensional lattice of configuration model networks with arbitrary total-degree distribution and inter-population mixing parameter $1-f$, shown as functions of the latter (Sec.V B): q^* (a), s^* (b), v^* (c), and D^* (d). The colored regions mark the range of each coefficient, which are bounded by the critical-region scaling ($T \gtrsim T_c$), and the limiting behavior ($T \gg T_c$), delineated by dashed and solid curves respectively; the former are straight lines, signifying agreement with the predicted scaling (17). Each panel's arrow indicates the direction of increase in the distance from the phase transition, $T/T_c - 1$.

and

$$D^* = \frac{TG''(1)}{2G'(1)}(1-f)\cosh(q^*) \tag{20}$$

where q^* satisfies (15), and v^* is given by the basic reproductive number multiplied by the average product of relative position, n, and incidence, $-\Delta n e^{-\Delta n q^*}$, on the end of a randomly selected edge. Fig. 3 shows the transport coefficients, (18), (19), and (20), as functions of T/T_c and f, with partial scaling collapse (17) for the corresponding class of network configurations. The expected reaction-diffusion scaling can be observed near the critical point, and far away from the critical region, when $T \gg T_c$, q^*, $\frac{s^*G'(1)}{TG''(1)}$, $\frac{v^*G'(1)}{TG''(1)}$, and $\frac{D^*G'(1)}{TG''(1)}$ tend to limiting curves which depend only on $1-f$, suggesting the intuitive asymptotic proportionality to the reproductive number.

C. Pulled Front Classification

In order to connect the transport properties of the linear equations to the full nonlinear system, we refer to the classification of fronts propagating into unstable states, which in our system is the fully susceptible metapopulation lying ahead of the infection front. In general, there are two types of deterministic fronts: pulled and pushed, with the former having fronts with asymptotic speed equal to the linear spreading speed and the latter having fronts with asymptotic speed greater than the linear spreading speed [22]. Pushed fronts occur because nonlinearities in the equations of motion tend to increase the growth of perturbations on the unstable state, resulting in nontrivial front shape dependence of the speed. However, in our system all nonlinearities are proportional to probability generating functions, $\sim G'(\theta)/G'(1)$ (11), which are monotonically increasing over the unit interval. Therefore, all nonlinearities tend to increase θ, and consequently dampen the growth of infection – a sufficient condition for pulled fronts [23], and thus we anticipate fronts in this model to be pulled; this agrees with the intuition that epidemic propagation is governed by its behavior in a fully susceptible population. In practice, the classification has importance for control strategies in systems with similar structure, implying that to mitigate the spread of infection among populations, efforts should be focused on the leading edge of the front, and not on larger outbreaks occurring farther behind.

D. Relaxation Properties

In addition to quantifying the transport, the front speed can be used to extract information about the dynamics away from the unstable state. As shown above, the $\vec{\theta}$-field settles onto a solution with translational similarity, $\vec{\theta}_{n\pm x}(t) = \vec{\theta}_n(t \mp \frac{x}{v^*})$, after an initial transient period. Behind the leading edge of the front, the behavior resembles a relaxation to the stable equilibrium (9), $\vec{\theta}_n(t) \approx \vec{\bar{\theta}} + \vec{\eta}(t - \frac{n}{v^*}) \approx \vec{\bar{\theta}} + \vec{\eta} e^{-z^*(n - v^* t)}$, where the spatial rate, $|z^*|$, is the dominant

eigenvalue of the nonlinear eigenvalue equation

$$\det\left(\underline{\underline{G'_e}}(\vec{\bar{\theta}}, z^*) - \frac{1+v^*z^*}{T}\underline{\underline{I}}\right) = 0, \quad \text{with} \tag{21}$$

$$\underline{\underline{G'_e}}(\vec{\bar{\theta}}, z) = \left[\begin{array}{ccc} \frac{G_{00}}{G_0(\vec{1})} & \frac{G_{0+}}{G_0(\vec{1})} & \frac{G_{0-}}{G_0(\vec{1})} \\ \frac{G_{-0}}{G_-(\vec{1})}e^{-z} & \frac{G_{-+}}{G_-(\vec{1})}e^{-z} & \frac{G_{--}}{G_-(\vec{1})}e^{-z} \\ \frac{G_{+0}}{G_+(\vec{1})}e^{z} & \frac{G_{++}}{G_+(\vec{1})}e^{z} & \frac{G_{+-}}{G_+(\vec{1})}e^{z} \end{array}\right]\Bigg|_{\vec{\bar{\theta}}} .$$

The latter is the analogue of $\underline{\underline{K_e}}(q)$ at the stable state, which does not depend on the first two moments of the degree distribution directly, but on the generating function's properties near the equilibrium (9). In general, the two characteristic spatial rates for this system are not equal, $|z^*| \neq q^*$, and when their difference is large, it typically signifies a significant separation in the time scales of growth, $1/s^*$, and relaxation $1/\left(v^*|z^*|\right)$. The latter provides an estimate for the amount of time a site is infectious, with $1/|z^*|$ yielding a related estimate for the width of the propagating front (i.e., the typical spatial extent of an outbreak at a given time). In particular, when the front speed is very fast and the degree distribution's second moments are large with the first moments $\mathcal{O}(1)$, we find that $|z^*| \ll q^*$, which suggests broad front profiles. In this case, propagation and relaxation can be thought of as approximately distinct processes. This has practical implications, because if such separation occurs, it implies that detecting an epidemic by measuring a finite infection level locally is a poor strategy for control – by the time detection has occurred, the front has propagated far away and started many other large outbreaks.

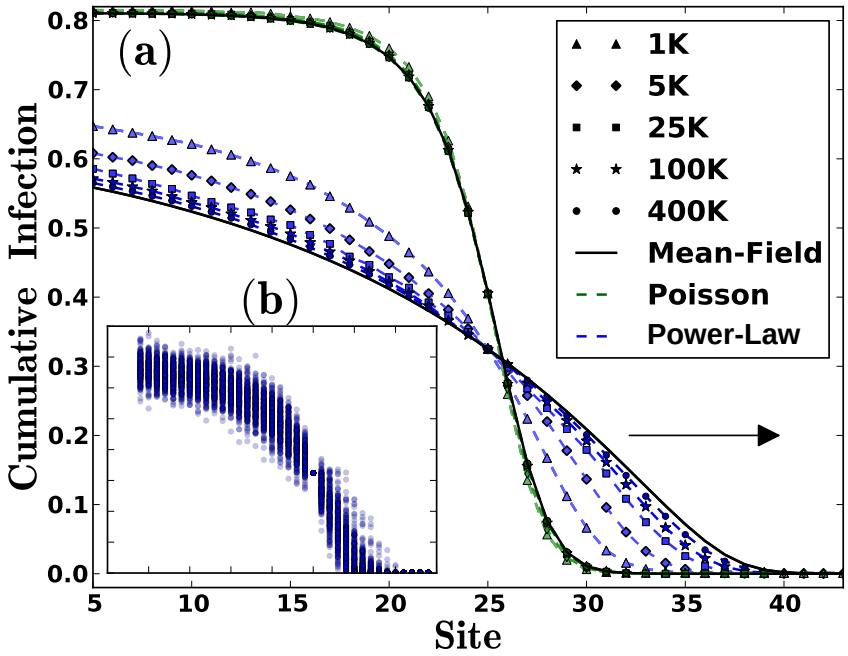

Figure 4: (a) A comparison between the average cumulative infection profile for stochastic simulations of SIR dynamics on a one-dimensional lattice of power-law (blue) and Poisson (green) networks and mean-field predictions (11). Various site sizes are shown with different symbols and color shades – varying from light to dark for 10^3 to 4×10^5 respectively. Front shapes for increasingly large sizes are found to converge to the respective mean-field front. The parameters for the underlying graphs were chosen to be: $K = 100$, $\alpha = 2$ and $p = 0.3$ for the power-law, and $C = 2.90157$ and $p = 0.3$ for the Poisson (Sec.VI). A lattice size of 50 sites was used, which was large enough to ensure uniformity with the above graph parameters and reaction rates $\beta = \gamma = 1$. The arrow indicates the propagation direction. (b) Stochastic front realizations conditioned on the middle lattice site having cumulative infection equal to half the equilibrium value (9). Averaging over realizations produced profiles like those in (a).

VI. Comparison with Stochastic Simulations

The above predictions for the mean-field dynamics on the one-dimensional metapopulation were compared to stochastic simulations of SIR dynamics on random instances of multi-scale, metapopulation networks, using Gillespie's Direct Method [19, 28, 29]. The graphs were constructed using the multitype configuration model by first generating a degree sequence from the desired degree distribution and then connecting pairs of edge-"stubs", selected uniformly at random [2, 4, 9]. An outbreak was started by choosing one node from the first lattice site to be infected with all others susceptible. Only outbreaks which lead to epidemics with $\mathcal{O}(N)$ cumulative infection were considered for comparison with mean-field predictions. In order to

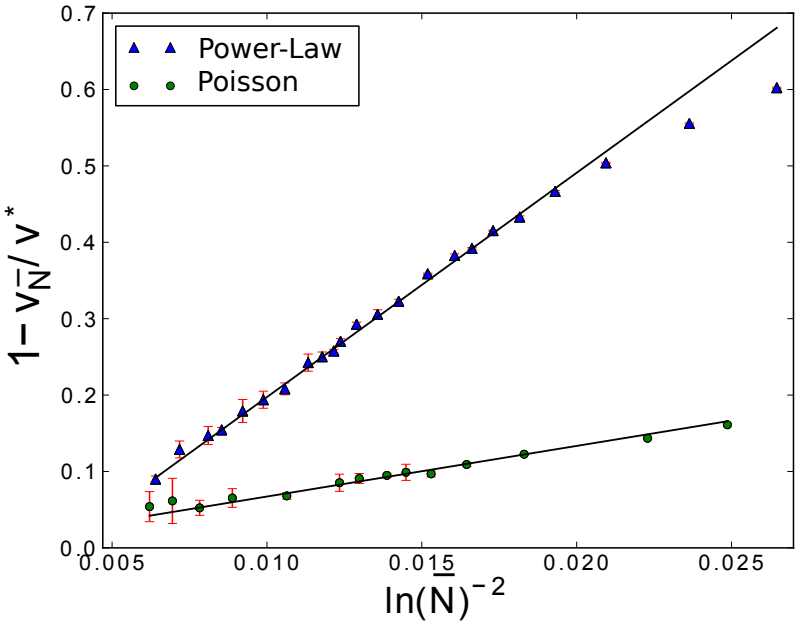

Figure 5: (a) Convergence of the average velocities, $v_{\bar{N}}$, to the mean-field predictions, v^*, for power-law (blue) and Poisson (green) networks (Fig. 4) as functions of the cumulative number of infected nodes at each site, shown with fits to the expected pulled front scaling, $v^* - v_{\bar{N}} \sim \frac{D^* q^* \pi^2}{\ln^2(\bar{N})}$(Sec.VI).

ignore fluctuations in the initial transients, time was zeroed after the first 100 reactions.

We are interested in the average shape of the front that connects the fully susceptible unstable state lying ahead of the infectious wave and the fully recovered (equilibrium) state lying behind it. The average shape was computed by taking instantaneous "snapshots" of the profile for each stochastic realization, conditioned on the middle lattice site having cumulative infection equal to half the equilibrium value (9), and averaging the cumulative infection of the other sites over different realizations. In general, the "snapshots" did not occur at the same instant; however, the shifting of different front realizations in time, such that they overlapped at a given point, and conditionally averaging over the shape, eliminated some of the effects of diffusive wandering. The measured fronts were compared to the mean-field profiles by integrating the lattice equations (11). A comparison is shown in Fig. 4 for two graphs with power-law and Poisson degree distributions, with generating functions

$$G_{P.L.}(\vec{x}) = \mathrm{Li}_\alpha \left(e^{-1/K} x_0 \left(1 - p + p x_+\right) \left(1 - p + p x_-\right) \right)$$

and

$$G_P(\vec{x}) = \exp\left(C\left(x_0\left(1-p+px_+\right)\left(1-p+px_-\right)-1\right)\right) \ ,$$

where Li_α is the polylogarithm function with exponent α [2]. The parameters for the degree distributions were chosen such that each network had the same average degree and cloning parameter, p (i.e., given a specified internal degree distribution, each of a node's internal edges is copied to form an external edge with probability p), but with different inherent levels of heterogeneity.

We see in Fig. 4 that the epidemic front is broader in the power-law network than in the Poisson[5]. This difference comes from the much larger front speed of the former, which had average excess degrees an order of magnitude larger than the latter, (12) and (15), and the relatively similar relaxation times (21) for the two classes of networks (implying that the time scale over which a site is infectious in each network is roughly the same). In the more homogeneous Poisson networks, the front is significantly more narrow and propagates through the lattice on the same time scales as the local infection dynamics; whereas in the power-law case, the leading edge of the front propagates very quickly through the lattice, followed by a slow relaxation to the stable equilibrium state behind the front – leaving many sites with large infection levels simultaneously. This comparison shows that assumptions of homogeneity can drastically underestimate the speed and extent of fronts in systems with heterogeneous and correlated interactions.

Additionally, the front speed v was numerically estimated from the average time $\langle\tau_{prog}\rangle$ required for the leading edge of the front to move forward by one lattice site (where the leading edge was defined as that site where the incidence first reached a set $\mathcal{O}(1)$ level) and averaging over such levels; i.e., $1/v = \langle\tau_{prog}\rangle$, once the initial spatial variation had decayed. Fig. 5 shows

[5] The effects are more drastic if a larger exponential cut-off is used.

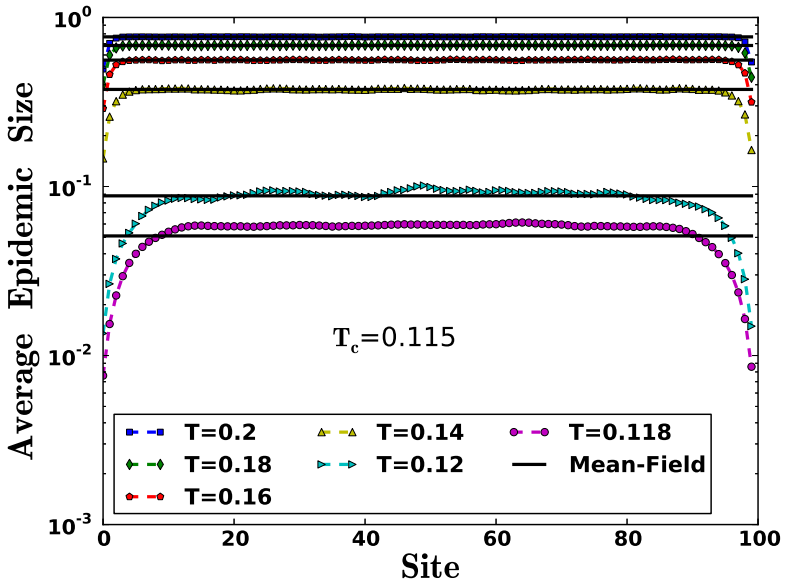

Figure 6: The average epidemic fraction at each site for a network with asymmetric generating function (Sec.VI) and varying transmissibilities. The critical point at which the epidemic vanished agrees with the prediction, $T_c = 0.115$ (13). Each site was occupied by 20,000 nodes on a lattice of 100 sites.

the convergence of the measured speed from simulations to the mean-field prediction for each graph as a function of the steady state, cumulative infected population size at every lattice site, $\bar{N} = \bar{P}N$ (Sec.III), with total size N. The lines represent fits to the expected scaling of the largest finite-size correction for pulled fronts, $v^* - v_{\bar{N}} \sim \frac{D^* q^* \pi^2}{\ln^2(\bar{N})}$, obtained from a general $1/\bar{N}$ cutoff in the mean-field equations [21–23]; the coefficients are found to be $\mathcal{O}(1)$ of the expected scaling. In general, higher order corrections in $\bar{N}$ must be calculated from an analysis of the full, stochastic system [23]. The very slow convergence in $\bar{N}$ comes from the transport dependence on the linearized equations where infinitesimal infection levels apply and sensitivity to stochastic effects is highest. This can be seen in the fairly large finite-size corrections to the velocity, particularly for the power-law network, leading to a more narrow conditionally averaged front relative to the mean-field, with fewer sites initiated at a given time (Fig. 4).

Finally, the average epidemic profile and transmissibility threshold, (9) and (13), were compared to simulations. Fig. 6 plots those comparisons for a system with left-right asymmetric

generating function

$$G_{Asym}(\vec{x}) = \frac{1}{3}\left(2x_0^2x_+^2x_-^4 + x_0^4x_+^6x_-^2\right) \ ,$$

on a lattice of 100 sites, with 20,000 nodes on each site. Both the epidemic size for various transmissibilities and the threshold were found to be in good agreement with mean-field predictions, though the finite-size effects became increasingly important as the critical region was approached, leading to significantly smaller outbreaks near the edges of the lattice.

VII. Conclusion

In this work we have constructed a mean-field theory for infection dynamics on multitype networks, and used such networks to model multiscale metapopulations. Together, this enabled us to explore how macro-scale disease propagation depends on micro-scale interaction structure. As a necessary first step in this direction, we applied the approach to a simple metapopulation model for a chain of coupled populations, and derived the transport properties for infection, including their scaling with the disease transmissibility and the statistical properties of the underlying network. We also found a threshold for the viability of epidemics, and calculated the relaxation properties of the propagating front. These were compared for different network models, with heterogeneous networks having considerably higher speeds and broader fronts than their homogeneous counterparts – illustrating the importance of including complexity in the fine-scale topology in order to accurately capture transport phenomenology, and demonstrating that long-range transport is not necessary for supporting fast propagation of epidemics.

Various extensions of the work presented – both in terms of analyses carried out and systems studied – could be considered. We have addressed here only the average dynamics of the one-dimensional, homogeneous system, without any description of finite-size fluctuations, or consideration of the dynamics in higher-dimensional generalizations (which we believe can be

analyzed in a similar way). Greater complexity could be introduced through the spatio-temporal dependence of network parameters, and/or more general network configurations [26] [6]. An interesting extension of the model discussed here would include dynamic contacts between nodes and explicit mobility, instead of the assumed time scale separation between topology and the overlying process [30, 32, 49]. However, the basic formalism presented here can enable one to study such factors and build more realistic models for infectious processes in multiscale problems.

[6] For example, we could use a similar analysis to study seasonally forced epidemics, which have oscillatory behavior somewhat akin to Parts III-IV

Part III

DRIVEN SYNCHRONIZATION IN RANDOM NETWORKS OF OSCILLATORS

Summary: Synchronization is a universal phenomenon found in many non-equilibrium systems. Much recent interest in this area has overlapped with the study of complex networks, where a major focus is determining how a system's connectivity patterns affect the types of behavior that it can produce. Thus far, modeling efforts have focused on the tendency of networks of oscillators to mutually synchronize themselves, with less emphasis on the effects of external driving. In this work we discuss the interplay between mutual and driven synchronization in networks of phase oscillators of the Kuramoto type, and explore how the structure and emergence of such states depends on the underlying network topology for simple random networks with a given degree distribution. We find a variety of interesting dynamical behaviors, including bifurcations and bistability patterns that are qualitatively different for heterogeneous and homogeneous networks, and which are separated by a Takens-Bogdanov-Cusp singularity in the parameter region where the coupling strength between oscillators is weak. Our analysis is connected to the underlying dynamics of oscillator clusters for important states and transitions [7].

[7] The material in Part III is reproduced from [72]

VIII. Introduction

The tendency for populations of oscillators to synchronize their dynamics and produce large-scale collective oscillations is relevant in a wide range of contexts [34–36]. A particularly simple class of models for this behavior was proposed by Kuramoto, where each oscillator in a network is described by a phase variable, which has a tendency to oscillate at its natural frequency and in phase with its neighbors [37]. This model has given insights into the dynamics of many systems, from the synchronization of coupled chemical oscillators and Josephson junction arrays, to correlations in visual cortex experiments and coherence in neutrino flavor oscillations [38–41].

Much recent work on the Kuramoto model has concerned synchronization on complex networks, where the transition to coherent oscillations depends on the properties of the network topology [42–44]. Some important results are vanishing synchronization thresholds and explosive transitions for networks with large degree fluctuations [43, 45, 46]. However, the effects of external driving are much less known, and questions about how different networks of oscillators respond to driving, and to what extent they can be controlled, have not been answered, even though in many circumstances, external fields are present [49]. An important example is the network of pacemaker cells, which play a role in determining mammalian circadian rhythms, and can be driven by light-dark cycles [48, 50, 56].

In what follows, we discuss the *interplay between mutual and driven synchronization* in random networks of phase oscillators with a given degree distribution. In particular, we present key aspects of the stability diagram for the driven Kuramoto model on these networks, focusing on the appearance of a codimension-three Takens-Bogdanov-Cusp singularity in the parameter region where the coupling strength between oscillators is weak. This bifurcation description is used to explain various pathways to driven and mutual synchronization in terms of synchronized oscillator clusters and network topology.

IX. Mean-Field Reduction and Analysis

Kuramoto showed that a system of limit cycle oscillators, each near their own Hopf bifurcation, with weak coupling to their neighbors and fast amplitude equilibration, have the following simple equations of motion:

$$\frac{d\theta_i}{dt} = \omega_i + J\sum_j A_{ij}\sin(\theta_j - \theta_i), \tag{22}$$

where θ_i is the phase of the ith oscillator, with natural frequency ω_i, coupling strength J, and adjacency matrix for the interaction network A_{ij}. Under generic circumstances (e.g., when the natural frequencies are randomly assigned according to a symmetric and unimodal distribution without correlations to the topology), this system undergoes a critical transition from incoherence to mutual synchronization once the coupling strength exceeds a threshold, resulting in a fraction of the network oscillating at the average of the natural frequencies, and with a stationary phase distribution [34, 36, 47].

A simple extension of the Kuramoto model that includes a periodic driving force is given by [51–53]:

$$\frac{d\theta_i}{dt} = \omega_i + J\sum_j A_{ij}\sin(\theta_j - \theta_i) + E\sin(\Omega t - \theta_i), \tag{23}$$

with external field strength E and frequency Ω. With similar assumptions for the natural frequency distribution, we expect each term to have the following effects on the dynamics: the randomness in the frequencies causes oscillators to have disperse phases with monotonic build-up in time, the coupling tends to align the phases of neighbors in proportion to the number of connections in a local environment (which will vary across the network), and the driving field tends to force oscillators to move at the driving frequency and away from their natural frequencies. The interactions among these tendencies, both cooperative and competitive, will

depend on the magnitude of each term and the network topology, and therefore we expect an intricate dynamics with multiple behaviors and transitions [53].

A. Degree class dynamics

To clarify the dynamics, we attempt to find a reduced description of (23). For convenience, we study the phases in the co-moving frame of the driving, $\phi_i = \theta_i - \Omega t$:

$$\frac{d\phi_i}{dt} = \omega_i - \Omega + J\sum_j A_{ij}\sin(\phi_j - \phi_i) - E\sin(\phi_i), \tag{24}$$

and consider random networks with a given degree distribution, p_k, that specifies the fraction of oscillators with k neighbors. In particular, we will study the annealed limit of random networks explicitly, for which $A_{ij} = \frac{k_i k_j}{N\langle k\rangle}$, where k_i and k_j are drawn from p_k for a network of size N with average degree $\langle k\rangle$, but note that our results are in qualitative agreement with quenched models (such as the configuration model, Fig.10 [54])[8]. For annealed networks we find oscillator dynamics:

$$\frac{d\phi_i}{dt} = \omega_i - \Omega + Jk_i\mathcal{I}m\left[e^{-i\phi_i}\sum_j \frac{k_j e^{i\phi_j}}{N\langle k\rangle}\right] + E\mathcal{I}m\left[e^{-i\phi_i}\right], \tag{25}$$

from which we can define the complex order parameter

$$z = \sum_j \frac{k_j e^{i\phi_j}}{N\,\langle k\rangle}, \tag{26}$$

or the average interaction strength (both magnitude and phase) that an oscillator feels along an edge to its neighbors.

We are interested in the thermodynamic limit, $N \to \infty$, in which it is useful to consider the density of oscillators with phase ϕ at time t, given degree k and frequency ω, $\rho(\phi, t; k, \omega)$. This

[8] Part IV shows a more general technique that could be similarly applied.

probability density satisfies a continuity relation:

$$\frac{\partial \rho}{\partial t} = -\frac{\partial}{\partial \phi}\left[\left(\omega - \Omega + \frac{e^{-i\phi}}{2i}(Jkz + E) - \frac{e^{i\phi}}{2i}(Jk\bar{z} + E)\right)\rho\right] \tag{27}$$

with

$$z(t) = \sum_k \frac{kp_k}{\langle k \rangle} \int g(\omega)\rho(\phi, t; \omega, k)e^{i\phi} d\omega d\phi, \tag{28}$$

where $g(\omega)$ is the natural frequency distribution and $\bar{z}$ is the complex conjugate of z. In order to solve (27) we expand ρ into its Fourier components:

$$\rho(\phi, t; \omega, k) = \frac{1}{2\pi}\left[1 + \sum_{n=1}^{\infty} \alpha_n(t; \omega, k)e^{in\phi} + \text{c.c.}\right], \tag{29}$$

and look for simple power-series solutions of the form, $\alpha_n(t; \omega, k) = \alpha^n(t; \omega, k)$ – an ansatz which was proposed by Ott and Antonsen, and that is applicable in a wide array of Kuramoto model variants [55, 57, 58]. In this case it gives the dynamics for $\bar{\alpha}(t; \omega, k)$:

$$\frac{d\bar{\alpha}}{dt} = \frac{1}{2}\left[Jkz + E\right] + i\left(\omega - \Omega\right)\bar{\alpha} - \frac{1}{2}\left[Jk\bar{z} + E\right]\bar{\alpha}^2, \tag{30}$$

which completely specifies the order parameter:

$$z(t) = \sum_k \frac{kp_k}{\langle k \rangle} \int g(\omega)\bar{\alpha}(t; \omega, k) d\omega. \tag{31}$$

In addition, the dimensionality of the system can be further reduced by performing the natural frequency integral, for which we assume:

$$g(\omega) = \frac{\gamma}{\pi\left[\left(\omega - \omega_0\right)^2 + \gamma^2\right]}, \tag{32}$$

a Cauchy distribution with median ω_0 and scale γ. Generically, $\bar{\alpha}(\omega, k, t)$ has no poles in the upper-half of the complex ω-plane, and therefore we perform contour integration of (31) closed in this region [55], which reduces the integral to the residue at the pole $\omega_0 + i\gamma$:

$$z(t) = \sum_k \frac{kp_k}{\langle k \rangle} \bar{\alpha}(t; \omega_0 + i\gamma, k) \equiv \sum_k \frac{kp_k}{\langle k \rangle} a_k(t), \tag{33}$$

where

$$\frac{da_k}{d\tau} = \frac{1}{2}\big[\mathcal{J}kz + \mathcal{E}\big] - (1 + i\Delta)\, a_k - \frac{1}{2}\big[\mathcal{J}k\bar{z} + \mathcal{E}\big]a_k^2, \tag{34}$$

with the dimensionless time, $\tau = \gamma t$, and normalized parameters: $\mathcal{E} = E/\gamma$, $\mathcal{J} = J/\gamma$, and $\Delta = (\Omega - \omega_0)/\gamma$.

This is the fundamental equation for the thermodynamic limit of the forced Kuramoto model on annealed networks. The dynamics has been reduced to a description of the average contribution to the order parameter by nodes of degree k, with the size of the state-space equal to twice the number of degree classes. In the following, we will focus on networks that have power-law degree distributions with finite cutoffs and Poisson distributions,

$$p_k = \frac{k^{-s}}{\sum_{k'=1}^{K_{cut}} k'^{-s}} \quad \text{and} \quad p_k = \frac{e^{-\langle k \rangle}\langle k \rangle^k}{k!}, \tag{35}$$

respectively, though analytic results are given for arbitrary distributions. We will refer to the former as simply "power-law" for brevity, though the degree cutoff, K_{cut}, will be specified when pertinent. In general, the cutoff determines the dimensionality of the reduced system, and we find that its value is relevant for heterogeneous network behavior, where large degree nodes can contribute significantly to the dynamics.

B. Limiting states

First, we consider the states of mutual and driven synchronization in instructive limits. For instance, in the limit where $\mathcal{E} \to 0$, Eq.(34) describes an un-driven network, and has stable solutions corresponding to simple oscillations : $a_k = r_k(\tau)e^{-i\Delta\tau}$, $z = R(\tau)e^{-i\Delta\tau}$,

$$\frac{dr_k}{d\tau} = \frac{1}{2}\mathcal{J}kR\big[1 - r_k^2\big] - r_k, \tag{36}$$

which reproduces known results [58]. In particular for the frame where $\Omega = 0$, the network tends to a purely oscillating state at the average natural frequency ω_0, with some fixed r_k^*. In addition, the incoherent state, $r_k^* = 0$, has a linear stability exponent

$$\lambda_{ic} = \frac{\mathcal{J}\left\langle k^2\right\rangle}{2\left\langle k\right\rangle} - 1, \tag{37}$$

which implies a threshold for the onset of mutual synchronization in the absence of driving, $r_k^* \neq 0$, $\frac{\mathcal{J}_c\langle k^2\rangle}{2\langle k\rangle} = 1$. We consider situations where $\mathcal{J} > \mathcal{J}_c$, and a coherent mutually synchronized state is stable without forcing [43] [9].

On the other hand, in the limit where the driving frequency is equal to the average natural frequency, $\Delta \to 0$, Eq.(34) describes states of driven synchronization, where the network is oscillating at the driving frequency on average, with amplitudes given by the fixed points of the self-consistent equation:

$$R^* = \sum_k \frac{kp_k}{\langle k\rangle}\left(\frac{-1 + \sqrt{1 + \left(\mathcal{J}kR^* + \mathcal{E}\right)^2}}{\left(\mathcal{J}kR^* + \mathcal{E}\right)}\right), \tag{38}$$

and with a large number of nodes entrained to the driving. From (38) we can see that incoherence is not a solution when $\mathcal{E} \neq 0$, meaning that external driving always enforces some level of

[9] This will be satisfied for virtually any $\mathcal{J} > 0$, for random networks with power-law degree exponents less than three and large degree cut-offs.

coherent oscillations at its frequency. Moreover, multiple coherent solutions can exist depending on the parameter values.

C. Partial stability diagram

Next, we provide the results of a stability and partial[10] bifurcation analysis that delineates the boundaries between the limiting states and helps to explain how each can be converted into the other. The associated stability diagrams are somewhat complicated, and it is therefore useful to have the results in hand before proceeding to fill in the details. A quantitative discussion and analysis can be found in Sec.IX D that derives some of the results, with a broader summary of behaviors found in Sec.X A.

The schematic stability diagrams shown in Fig.7 illustrate two types of behavior in the $(\Delta, \mathcal{E})$ plane when the coupling, $\mathcal{J}$, is weak (Sec.IX D). If we consider networks with power-law degree distributions, Fig.7(a) shows the generic behavior when the degree exponent, s, is large. We find that this is maintained for networks with relatively homogeneous degree distributions, such as Erdős-Rényi, k-regular, or complete graphs [53]. Conversely when the degree exponent is small, i.e., the degree distribution has a heavy tail, the behavior looks like Fig.7(b). Because the former reproduces the behavior for the complete graph, and the latter occurs as the amount of variation in the degree distribution is increased, we distinguish these cases by the terms homogeneous and heterogeneous driven behavior.

[10] All of the unstable cycle bifurcations in the heterogeneous case have not yet been resolved. Furthermore for power-law networks with $k = 1, 2...K_{cut}$, when $\mathcal{J} \gtrsim 2.5$, additional SN curves emerge which complicate the unfolding shown in Fig.7 (See Sec. IX D).

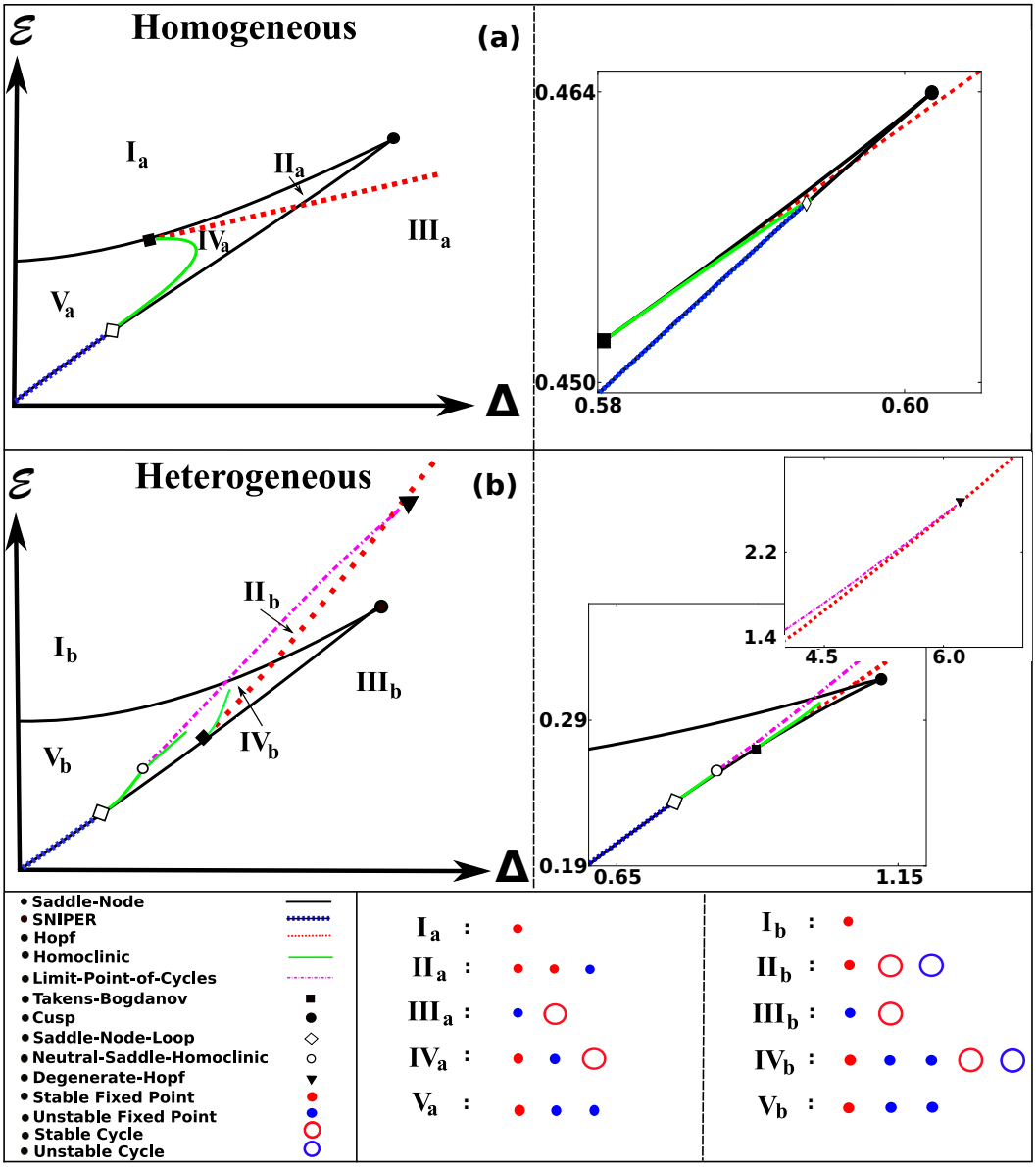

Figure 7: Stability diagrams for the driven Kuramoto model on random networks shown as functions of the driving field strength $\mathcal{E}$ and frequency detuning Δ. A legend is given in the bottom left. (a) Schematic diagram (left) for homogeneous behavior (e.g., power-laws with large exponents, k-regular, and Poisson degree distributions); (right) diagram for a power-law network with $\mathcal{J} = 2$, $s = 3.0$, and $K_{cut} = 200$. (b) Schematic partial diagram (left) for heterogeneous behavior (power-law degree distribution with small exponent), in the parameter region where $\mathcal{J}$ is weak (Sec.IX D); partial diagram for a power-law network with $\mathcal{J} = 0.25$, $s = 2.3$, and $K_{cut} = 1000$, shown in two parameter ranges for clarity. A table indicating possible states is shown in the bottom right for important regions (Roman numerals).

In particular, we find that the Takens-Bogdanov point appears on the upper branch of

the saddle-node bifurcations for the homogeneous case, but appears on the lower branch for the heterogeneous case, as depicted in Fig.7. The transition between the two behaviors can occur, for example, by decreasing the degree exponent, for some fixed $\mathcal{J}$ and K_{cut}, until the Takens-Bogdanov and cusp bifurcations are coincident, which typically occurs for some $2 \lesssim s \lesssim 3$ (see Sec.IX D for descriptions of these bifurcations). The existence of this singularity allows us to construct the behaviors shown through a combination of analytic results, numerical continuation, and general predictions for subsequent bifurcations. Details are given in the following sections, and example stability diagrams are shown alongside schematics in Fig.7.

D. Stability analysis and bifurcations

We begin constructing the stability diagrams by first finding the fixed points of Eq.(34), which denote states of driven synchronization, and establish how such states change stability. In general, fixed points satisfy $\frac{da_k}{d\tau} = 0$, which implies the self-consistent condition for z^*:

$$\begin{aligned} z^* &= \sum_k \frac{kp_k}{\langle k \rangle} a_k^* \\ &= \sum_k \frac{kp_k}{\langle k \rangle} \frac{-(1+i\Delta) + \sqrt{(1+i\Delta)^2 + |\mathcal{J}kz^* + \mathcal{E}|^2}}{\mathcal{J}k\bar{z}^* + \mathcal{E}}. \end{aligned} \tag{39}$$

Each a_k is a complex number, and so could be represented by a magnitude and phase, or with real and imaginary parts. Next, it is useful to consider how the dynamics respond to perturbations away from the steady-states given by (39), e.g. $\mathcal{R}e[a_k^*] + x_k$ and $\mathcal{I}m[a_k^*] + y_k$ where x_k and y_k are the k'th components of the right eigenvectors of (34) at a_k^*, in the real and imaginary part representation of a_k. Equivalently, we can define $\eta_k = \frac{1}{\sqrt{2}}(x_k + iy_k)$ and $\widetilde{\eta}_k = \frac{1}{\sqrt{2}}(x_k - iy_k)$, with the perturbations $a_k^* + \sqrt{2}\eta_k$ and $\bar{a}_k^* + \sqrt{2}\widetilde{\eta}_k$. It is more convenient to use the latter and leave Eq.(34) in its complex form, while keeping in mind that the standard results of bifurcation theory pertain to some underlying real representation of (34).

We look for the linear stability spectrum of eigen-modes around a fixed point by adding the perturbations discussed into (34), and collecting terms of order η:

$$\begin{aligned}\frac{d\eta_k}{d\tau} &= \frac{\mathcal{J}k}{2}\left[\sum_{k'}\frac{k'p_{k'}}{\langle k\rangle}\eta_{k'} - a_k^{*2}\sum_{k'}\frac{k'p_{k'}}{\langle k\rangle}\widetilde{\eta}_{k'}\right] - q_k^*\eta_k,\\ \frac{d\widetilde{\eta}_k}{d\tau} &= \frac{\mathcal{J}k}{2}\left[\sum_{k'}\frac{k'p_{k'}}{\langle k\rangle}\widetilde{\eta}_{k'} - \bar{a}_k^{*2}\sum_{k'}\frac{k'p_{k'}}{\langle k\rangle}\eta_{k'}\right] - \bar{q}_k^*\widetilde{\eta}_k,\end{aligned} \tag{40}$$

with

$$q_k^* = 1 + i\Delta + \left(\mathcal{J}k\bar{z}^* + \mathcal{E}\right)a_k^*; \tag{41}$$

This system has a set of solutions, $\frac{d\eta_k}{d\tau} = \lambda\eta_k$ and $\frac{d\widetilde{\eta}_k}{d\tau} = \lambda\widetilde{\eta}_k$, from which we can find a self-consistent equation for the spectrum $\{\lambda\}$. Solving for η_k and $\widetilde{\eta}_k$ in (40), multiplying by $\frac{kp_k}{\langle k\rangle}$, summing over k, and eliminating the constants $\sum_k \frac{kp_k}{\langle k\rangle}\eta_k$ and $\sum_k \frac{kp_k}{\langle k\rangle}\widetilde{\eta}_k$ gives:

$$\left[\frac{\sum_k \frac{\mathcal{J}k^2p_k a_k^{*2}}{2\langle k\rangle(\lambda+q_k^*)}}{\sum_k \frac{\mathcal{J}k^2p_k}{2\langle k\rangle(\lambda+q_k^*)} - 1}\right]\left[\frac{\sum_k \frac{\mathcal{J}k^2p_k \bar{a}_k^{*2}}{2\langle k\rangle(\lambda+\bar{q}_k^*)}}{\sum_k \frac{\mathcal{J}k^2p_k}{2\langle k\rangle(\lambda+\bar{q}_k^*)} - 1}\right] = 1. \tag{42}$$

Next, we catalogue relevant bifurcations found in Fig.7, and discuss their dynamical behaviors in Sec. X A. First, the spectrum condition can be used to find the local codimension-one bifurcations, where some number of eigenvalues cross the imaginary axis (codimension implying the number of parameters that must be changed in order for a bifurcation to occur) [59, 60]. The most generic such crossing is the saddle-node bifurcation (SN), in which the spectrum at the equilibrium has one simple zero eigenvalue, and at which two equilibrium points collide and

disappear:

$$\left| \left[\frac{\sum_k \frac{\mathcal{J}k^2 p_k {a_k^*}^2}{2\langle k\rangle q_k^*}}{\sum_k \frac{\mathcal{J}k^2 p_k}{2\langle k\rangle q_k^*} - 1} \right] \right|^2 = 1. \tag{43}$$

The SN condition (43) predicts when steady states of driven synchronization vanish, and signifies when a local barrier (represented by the saddle) in the dynamics has been overcome. Importantly, we find that the lower branch of SN bifurcations contains a section of saddle-node-infinite-period bifurcations ($SNIPER$) (e.g., crossing V-III in Fig.7), where an SN occurs on a limit cycle of infinite period [53].

Another local codimension-one bifurcation is the Hopf (H), in which the spectrum at the equilibrium has two purely imaginary eigenvalues, with all others having non-zero real parts. At this point the amplitude of a periodic orbit decreases continuously to zero with its period tending to $2\pi/\omega_H$, where $\lambda = i\omega_H$:

$$\left[\frac{\sum_k \frac{\mathcal{J}k^2 p_k {a_k^*}^2}{2\langle k\rangle (i\omega_H + q_k^*)}}{\sum_k \frac{\mathcal{J}k^2 p_k}{2\langle k\rangle (i\omega_H + q_k^*)} - 1} \right] \left[\frac{\sum_k \frac{\mathcal{J}k^2 p_k {\bar{a}_k^*}^2}{2\langle k\rangle (i\omega_H + \bar{q}_k^*)}}{\sum_k \frac{\mathcal{J}k^2 p_k}{2\langle k\rangle (i\omega_H + \bar{q}_k^*)} - 1} \right] = 1. \tag{44}$$

When the periodic orbit associated with the Hopf bifurcation is stable, it is called supercritical (H_{sup}), and when it is unstable, it is called subcritical (H_{sub}) [60, 61]. In contrast with homogeneous network behavior (e.g., crossing $\mathrm{I}_a - \mathrm{III}_a$ in Fig.7(a)) [53], both branches of cycle stability can appear if the degree distribution is broad enough (e.g., crossing $\mathrm{II}_b - \mathrm{III}_b$ in Fig.7(b)).

Beyond the local codimension-one bifurcations, there are two key local codimension-two bifurcations. These are important to unravel because they can inform us as to what global bifurcations occur. The first appears when two branches of the SN collide, in the neighborhood of which there exist three states of driven entrainment; this is known as a cusp (C) [61]. To find the C point, we first consider that near a bifurcation, the equations of motion can be restricted

to a center manifold with the same dimension as the number of eigenvectors whose eigenvalues cross the imaginary axis, and is tangent to those vectors. Furthermore, the dynamics of the center manifold are equivalent to the normal form for the bifurcation. In the simple case of a SN, the center manifold is one-dimensional, $m = w\eta + w^2 h + \mathcal{O}(w^3)$ with the normal form: $\frac{dw}{dt} = cw^2 + \mathcal{O}(w^3)$ [59, 61].

The C bifurcation occurs when $c = 0$, a condition for which can be found by substituting the center manifold expansion and normal form into (34), collecting terms of order w^2, and taking the complex inner product of the resulting vector, B, with the left eigenvectors, ζ [62]. The right and left eigenvectors are found from a similar self-consistent analysis as for (42), and in the complex representation are respectively:

$$\eta_k(\lambda) = \frac{A\mathcal{J}k}{2}\left(\frac{x(\lambda) - a_k^{*2}}{\lambda + q_k^*}\right) \tag{45}$$

$$\widetilde{\eta}_k(\lambda) = \frac{A\mathcal{J}k}{2}\left(\frac{1 - x(\lambda)\bar{a}_k^{*2}}{\lambda + \bar{q}_k^*}\right) \tag{46}$$

$$\zeta_k(\lambda) = \frac{Zkp_k}{\langle k\rangle}\left(\frac{x(\lambda)}{\left(\sum\limits_k \frac{\mathcal{J}k^2 p_k}{2\langle k\rangle(\lambda+\bar{q}_k^*)} - 1\right)\left(\lambda + \bar{q}_k^*\right)}\right) \tag{47}$$

$$\widetilde{\zeta}_k(\lambda) = \frac{Zkp_k}{\langle k\rangle}\left(\frac{1}{\left(\sum\limits_k \frac{\mathcal{J}k^2 p_k}{2\langle k\rangle(\lambda+q_k^*)} - 1\right)\left(\lambda + q_k^*\right)}\right), \tag{48}$$

with constants A and Z, and with the conveniently defined sum,

$$x(\lambda) = \left[\frac{\sum\limits_k \frac{\mathcal{J}k^2 p_k a_k^{*2}}{2\langle k\rangle(\lambda+q_k^*)}}{\sum\limits_k \frac{\mathcal{J}k^2 p_k}{2\langle k\rangle(\lambda+q_k^*)} - 1}\right]. \tag{49}$$

Collecting terms of order w^2 in the expansion produces the bilinear form for (34) evaluated at

the vector $\eta_k, \widetilde{\eta}_k$:

$$B_k(\lambda) = -2\mathcal{J}Ak\eta_k a_k^* - (\mathcal{J}k\bar{z}^* + \mathcal{E})\eta_k^2 \tag{50}$$

$$\widetilde{B}_k(\lambda) = -2\mathcal{J}Axk\widetilde{\eta}_k \bar{a}_k^* - (\mathcal{J}kz^* + \mathcal{E})\widetilde{\eta}_k^2. \tag{51}$$

Putting these together generates the normal form coefficient c, and a condition for the cusp bifurcation:

$$c = \sum_k \bar{\zeta}_k(0)B_k(0) + \bar{\widetilde{\zeta}}_k(0)\widetilde{B}_k(0) = 0, \tag{52}$$

in conjunction with (20).

It should be noted that for power-law networks with $\mathcal{J} \lesssim 2.5$, the number of possible fixed points for this system is three, which we call the weak coupling region. However, when the coupling is stronger, a degenerate C point seems to emerge, which generates additional unstable and saddle states, and complicates the unfolding (shown in Fig.7), though much of the general structure is maintained for larger $\mathcal{J}$. In this work, we restrict ourselves to the weak coupling region for power-law networks, because the comparison between homogeneous and heterogeneous graphs is more straightforward.

The second local codimension-two bifurcation is the Takens-Bogdanov (TB), at which the spectrum has a double root at zero. Attached to this bifurcation are curves of SN and H bifurcations as well as a curve of Homoclinic Bifurcations (HC) [61–65]. In the latter, the period of a cycle diverges as it collides with a saddle-point and connects its stable and unstable manifolds (e.g., crossing $\mathrm{IV}_a - \mathrm{V}_a$ in Fig.7(a)). To find the location of the TB bifurcation, we expand (44) in powers of ω_H, and enforce that terms of order ω_H vanish, which gives the

criterion:

$$\mathcal{R}e\left[\left(\sum_k \frac{\mathcal{J}k^2 p_k a_k^{*2}}{2\langle k\rangle q_k^{*2}}\right)\left(\sum_k \frac{\mathcal{J}k^2 p_k \bar{a}_k^{*2}}{2\langle k\rangle \bar{q}_k^{*}}\right) - \left(\sum_k \frac{\mathcal{J}k^2 p_k}{2\langle k\rangle q_k^{*2}}\right)\left(\sum_k \frac{\mathcal{J}k^2 p_k}{2\langle k\rangle \bar{q}_k^{*}} - 1\right)\right] = 0, \quad (53)$$

that in conjunction with (43), determines the bifurcation point.

Finally, the highest codimension bifurcation that we consider arises when the C collides with the TB (TBC), implying that (43), (52), and (77) are all satisfied (which also occurs in the Hodgkin-Huxley equations) [62, 65, 66]. In addition to the bifurcations discussed, this particular singularity predicts curves of codimension-two homoclinic bifurcations to Saddle-Node-Loops (SNL) and Neutral Saddles (NS), and curves of Degenerate Hopf bifurcations (DH). The latter two are termination points for curves of Limit-Point-of-Cycles (LPC). These bifurcations imply new behaviors that do not appear for homogeneous networks and have interesting effects on the dynamics. Specifically, the LPC transition entails that a stable cycle collides with an unstable cycle and disappears, while the DH entails that an LPC emerges on a H point – typically as the Lyapunov exponent of the Hopf cycle vanishes. Because these bifurcations only occur when the TB is on the lower branch of the SN, they are not seen in homogeneous networks. Lastly, the SNL and NS entail that a homoclinic cycle is coincident with a SN and a saddle whose whose eigenvalues sum to zero, respectively [61, 62, 64–66] (see Fig.7).

X. Oscillator Dynamics

In this section, we explore some of the implications of the behaviors discussed on the dynamics of driven homogeneous and heterogeneous networks. Both the mean-field (Eq.34) and oscillator (Eq.24) dynamics are examined.

A. Key transitions and bistability

First, we can distill from the above that there are three primary ways that a stable mutually synchronized state can be created: H_{sup}, $SNIPER$, and LPC transitions. Qualitatively, we can think of such states as limit cycles, and can consider how their average amplitude and frequency (inverse period) emerge through each transition. If we imagine changing one parameter (e.g. $\mathcal{E}$), one of three things happens: the amplitude can appear continuously with a discontinuous frequency (H_{sup}), the amplitude can appear discontinuously with continuous frequency ($SNIPER$), or the amplitude and frequency can both appear discontinuously (LPC). The special case of continuous amplitude and frequency appearance occurs through a TB bifurcation. Fig.8 shows a comparison between the behaviors of mutually synchronized states produced by crossing these transitions.

Interestingly, we find that each transition has a signature in the average phase build-up with respect to the driving field. For example if the $SNIPER$ transition is crossed (e.g., crossing V $-$ III in Fig.7), the order-parameter dynamics is a large limit cycle that includes the origin [53]. This implies that the average phase of the network grows monotonically with respect to the field, and is therefore largely depinned from it, with a macroscopic number of nodes lapping it continually. Moreover, this behavior holds widely for degree classes as well – most degrees continually lap the field on average, perhaps excluding low degree nodes (e.g., k=1 or 2) depending on the parameters (Fig.8(b)). On the other hand if the H_{sup} is crossed (e.g., crossing I $-$ III in Fig.7), a small limit cycle emerges, centered around an unstable driven state. In this case there is no net build-up of the average phase with respect to the field; the motion is analogous to quasi-periodicity with average frequency equal to the driving, and an emergent "wobble" frequency given by (44) [53]. This behavior holds for all degree classes, implying that large and small degrees on average both have phase-trapped dynamics (Fig.8 (a)). However if the LPC transition is crossed (e.g., crossing $\mathrm{I}_b - \mathrm{II}_b$ in Fig.7(b)), a large cycle emerges for

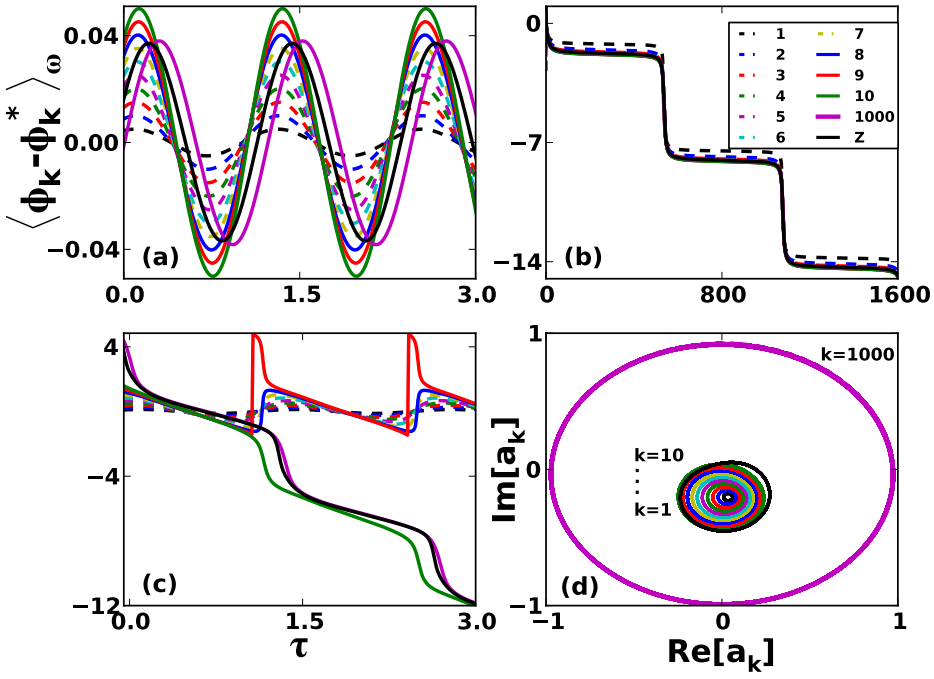

Figure 8: Comparison of mutually synchronized states that arise from perturbations to driven states just below the key transitions for networks with power-law degree distributions. Subplots (a-c) show the average phase deflection from a driven state for various degree classes versus time; colors for every degree class are specified in (b). (a) Below a H_{sup}: $\mathcal{E} = \mathcal{E}_H - 10^{-4}$, $\Delta = 5.5$, $\mathcal{J} = 0.25$, $s = 2.6$, and $K_{cut} = 1000$; the state appears with finite frequency and small amplitude. (b) Below a $SNIPER$: $\mathcal{E} = \mathcal{E}_{SN} - 10^{-4}$, $\Delta = 0.2$, $\mathcal{J} = 0.25$, $s = 2.3$, and $K_{cut} = 1000$; the state appears with a large period and with all degree classes increasing phase monotonically with respect to the field. (c) Below a LPC (below H_{sub}): $\mathcal{E} = \mathcal{E}_H - 10^{-4}$, $\Delta = 5.5$, $\mathcal{J} = 0.25$, $s = 2.3$, and $K_{cut} = 1000$; the state appears with finite frequency and large amplitude, and with high degree nodes increasing phase monotonically with respect to the field (phase-slip motion), while small degree nodes remain phase-trapped (on average). (d) Mutually synchronized state of (34) with (c) parameter values, illustrating the cycle size variation with degree for states produced by crossing the LPC transition.

the order-parameter that includes the origin (similar to the SNIPER), but only holds for nodes with large degree on average, i.e., nodes of small degree undergo phase-trapped motion, while nodes of large degree undergo phase-slip motion (Fig.8(c)). If we consider moving up the LPC by increasing $\mathcal{E}$, more and more high degree nodes become trapped by the field, until all are trapped, and the H_{sup} occurs – the opposite limit brings us to the lower $SNIPER$ (see Fig.7).

Another important difference between heterogeneous and homogeneous behavior concerns the bistability of driven and mutually synchronized states. Phase portraits are given in Fig.9, projected onto the order parameter, which demonstrate the behavior in important parameter regions. For homogeneous networks, bistability exists in a small region of parameter space,

confined between the C and HC bifurcations (i.e., regions II_a and IV_a in Fig.7(a)). In this case, there is bistability between two states of driven synchronization (region II_a and Fig.9(a)), until the H_{sup} is crossed (e.g., crossing $\mathrm{II}_a - \mathrm{IV}_a$), and bistability between a state of quasi-periodic mutual synchronization and driven synchronization (Fig.9(b)) [53]. In both cases, the manifolds of the saddle act as a separatrix between the two stable states. In contrast, for heterogeneous networks there is only bistability between a large-amplitude state of mutual synchronization and a single state of driven synchronization. The mutually synchronized state encloses all three fixed points in region IV_b (Fig.7(b) and Fig.9(d)), and exists in an additional region that does not contain a saddle (II_b in Fig.7(b) and Fig.9(c)). An example comparison of the bistability in finite network simulations for the two types of behavior is shown in Fig.10.

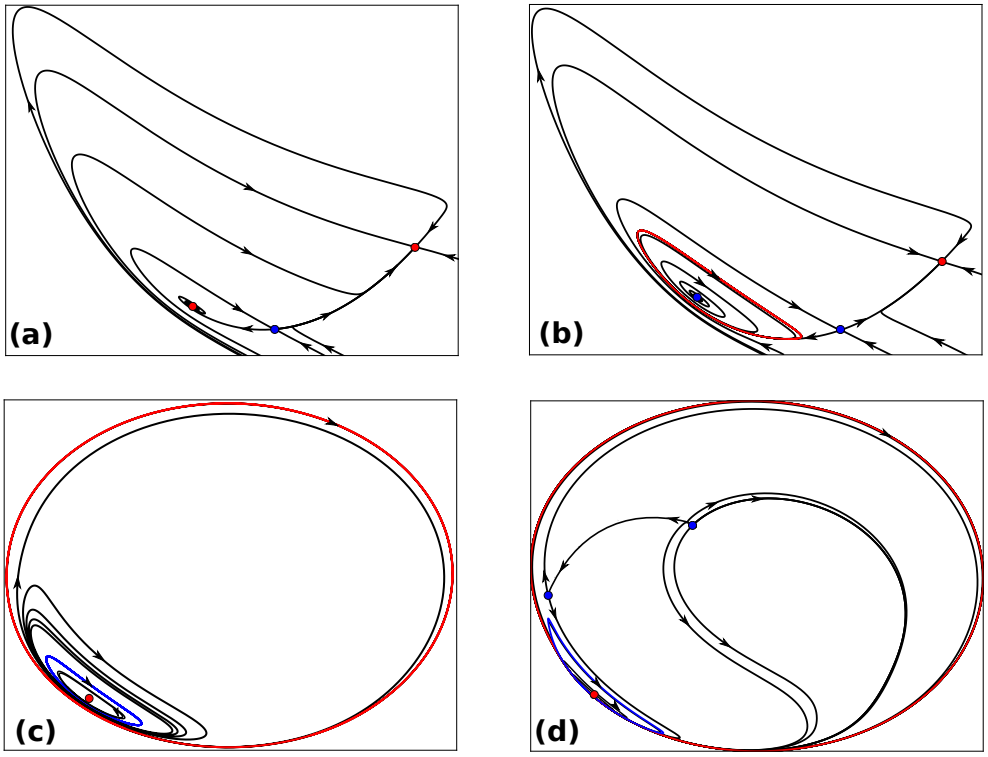

Figure 9: Phase portraits of the dynamics projected onto the complex plane of the order parameter for bistability regions (II_a, IV_a, II_b, and IV_b, shown in (a),(b),(c), and (d), respectively). Initial transients were ignored, and curves were plotted once an effective two-dimensional dynamics was seen. The colors red and blue denote stable and unstable fixed points and cycles, respectively. Panels have been rotated and scaled for clarity.

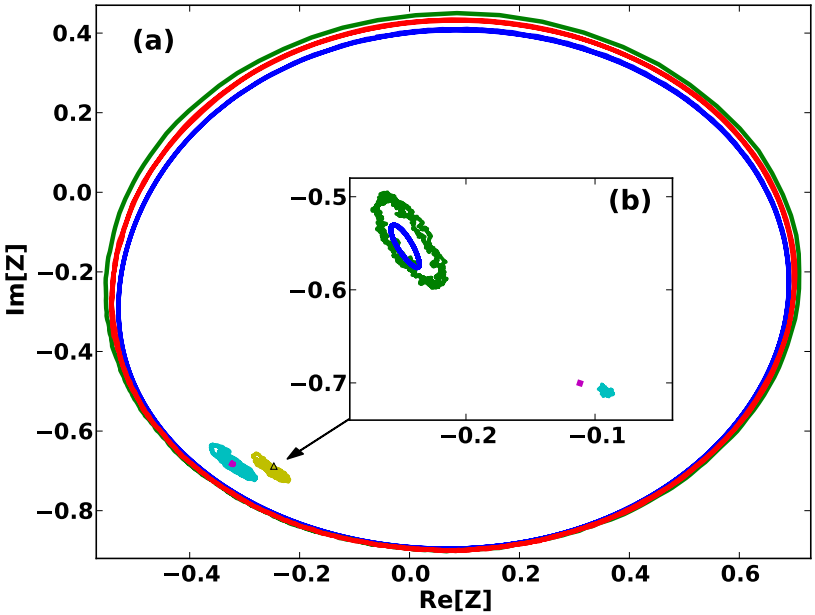

Figure 10: Comparison of bistability of mutual and driven synchronization on heterogeneous and homogeneous networks. (a) Stable states for a network with power-law degree distribution: $\mathcal{E} = 7.1$, $\Delta = 8.0$, $\mathcal{J} = 2.0$, $s = 2.0$, and $K_{cut} = 200$; the order parameter (57) is shown for the mean-field cycle (blue), annealed cycle (green), configuration-model cycle (red), mean-field equilibrium (magenta), annealed equilibrium (cyan), and configuration-model equilibrium (yellow with triangle), with good agreement among the respective states (region II_b in Fig. 7 (b)). Networks consist of 30,000 nodes. (b) Analogous plot for a Poisson degree distribution network with the same average degree as (a) and with $\mathcal{J} = 0.75$; $\mathcal{E} = 2.27$, $\Delta = 2.1216$ for the mean-field, and $\mathcal{E} = 2.3$, $\Delta = 2.134$ for the annealed (region IV_a in Fig. 7 (a)) [71]. The arrow indicates where (b) can be found in z's complex plane for comparison with (a).

B. Cluster behavior

Finally, we are interested in how the states and transitions discussed in the previous sections appear at a finer scale of resolution: the dynamics of oscillator clusters in the network. For stable states of driven synchronization, we find a single macroscopic cluster of phase-locked nodes, which are entrained to the driving and are stationary in the co-moving frame (labeled "L" in Fig.11(a)). This cluster is comprised of oscillators that have natural frequencies near the driving, with frequency ranges for degree classes that typically increase with degree, so that higher degree classes are able to stabilize a broader range of frequencies. Moreover, nodes with natural frequencies outside of their degree class's locked range have average velocities (time average of Eq.(24)) that are monotonically increasing with the displacement from that range,

and thus lap the driving field continually with disperse phases from one another. We therefore call these oscillators "winding" (labeled "W" in Fig.11(a)). The average velocities of phase-locked and winding nodes are shown in Fig.11(a) for a driven state as functions of their degrees and natural frequencies.

On the other hand, a stable state of mutual synchronization has a macroscopic cluster of nodes which lap the field together at some emergent average velocity. In addition, there exist other large "plateau" clusters of higher harmonics with average velocities that are integer multiples of the fundamental velocity, and therefore lap the driving field $2, 3, 4...$ times in one network cycle (labeled as $1, 2...$ in Fig.11(b)). Collectively these harmonic plateaus drive phase-trapped nodes at a frequency equal to the fundamental velocity, causing them to wobble around the driving-field, but with average velocity zero (labeled 0 in Fig.11(b)). The last group of oscillators, which are between the plateaus, wind with average velocities that grow monotonically with the displacement from a given plateau, and have disperse phases. This picture is consistent with general results for Kuramoto models, in which devil's staircases do not appear, and velocities strictly increase between plateaus [67, 68]. Fig.11(b) shows a typical velocity profile for a mutually synchronized state.

Since we find that an important difference between driven and mutually synchronized states is the appearance of plateaus in the velocity profile, we would like know how the plateaus are occupied when crossing the key transitions[51]. For instance, in crossing over a $SNIPER$ transition, we find that the plateaus of the mutually synchronized state emerge from the phase-locked cluster of a driven state, as a finite fraction of locked nodes with natural frequencies near the average break away from the external field (shown in Fig.12(a-b)). This is consistent with the depinning, continuous frequency and discontinuous amplitude appearance predicted by the mean-field dynamics. Conversely when crossing over the H_{sup}, we find that a small stable cluster of winding nodes in a driven state, with natural frequencies near the average, coalesce around the same average velocity (44), and form the first plateau. As the transition is approached

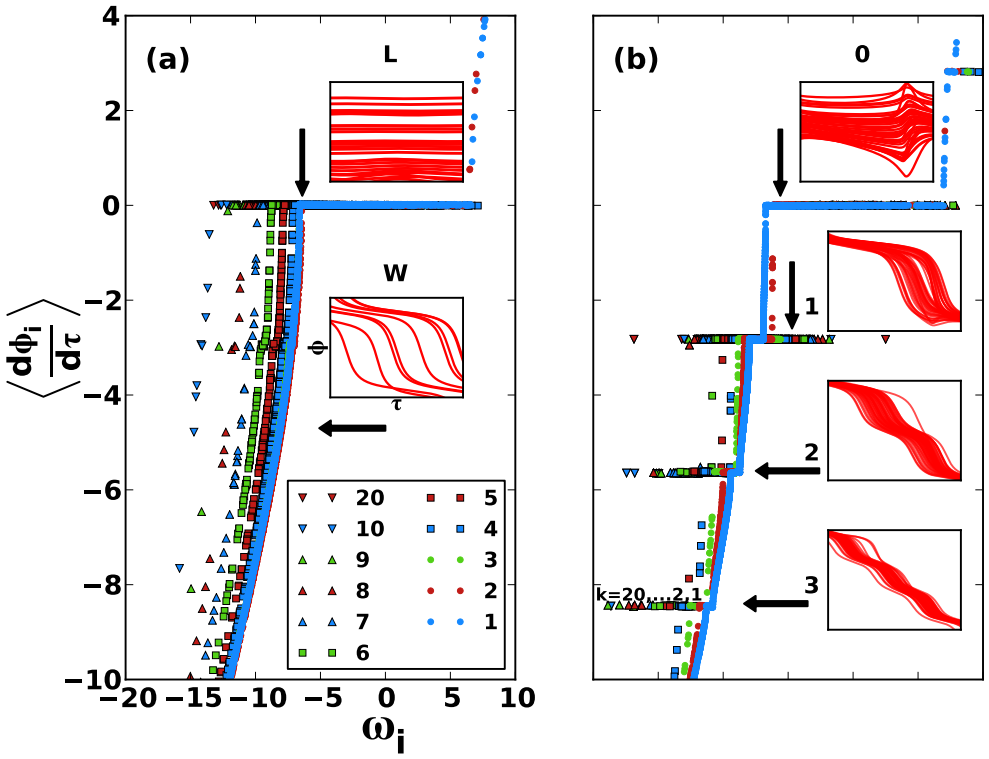

Figure 11: The average velocities for a network with a power-law degree distribution shown versus natural frequency. (a) A stable state of driven synchronization. (b) A stable state of mutual synchronization. The parameters are $\mathcal{E} = 7.1$, $\Delta = 8.0$, $\mathcal{J} = 2.0$, $s = 2.0$, $K_{cut} = 200$, and $N = 30000$ at which (a) or (b) can be realized, given appropriate initial conditions (region II_b in Fig.7(b)). The inset panels for (b) show ϕ_i vs. τ over one cycle with ranges [0,-π], [0,-2π], [0,-4π], and [0,-6π] for the plateau numbers $n = 0, 1, 2$, and 3, respectively. The node types for (a) are labeled "L" for locked "W" for winding, and appear next to the inset panels. Also, arrows indicate which cluster of oscillators are shown. A color legend for degree is given in (a).

the size of each plateau goes to zero (shown in Fig.12(c-d)). This produces the discontinuous frequency and continuous amplitude limit cycle with quasi-periodicity described by the mean-field H bifurcation. Different still, when crossing over the LPC, we find that a large group of nodes, which could form the winding and locked clusters of a driven state, can coalesce around an average velocity instead (given appropriate initial conditions). This produces an additional stable state of mutual synchronization that is bistable with the driven state, and has plateaus that are disproportionately occupied by high degree classes. The velocities and order parameter dynamics are compared in Fig.11 and Fig.10(a) for these bistable states, respectively.

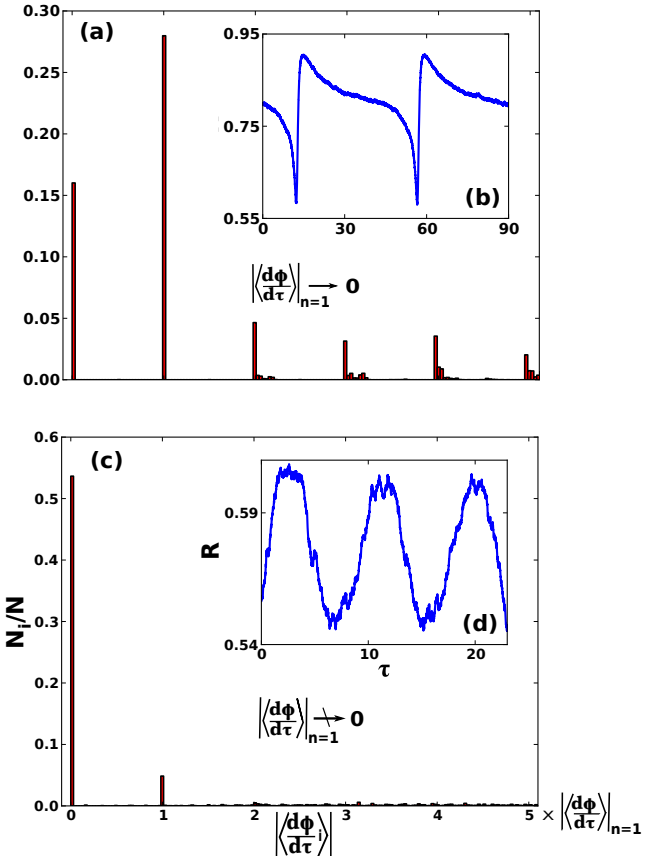

Figure 12: (a) A histogram of the average speeds for a network with a power-law degree distribution just below a $SNIPER$ transition. The parameters are $\mathcal{E} = 3.61$, $\Delta = 4.0$, $\mathcal{J} = 2.0$, $s = 2.0$, $K_{cut} = 200$, and $N = 30000$. We can see that roughly 30% of the network becomes depinned and forms the first plateau, which has speed ($|\left\langle \frac{d\phi}{d\tau} \right\rangle|_{n=1} \to 0$). (b) The magnitude of the order parameter as a function of time, displaying relaxation dynamics as the network slows down in the neighborhood of a driven state that vanished in the transition. (c) Analogous histogram for a Poisson degree distribution network with the same average degree as (a), but just below a H_{sup} transition with parameters $\mathcal{E} = 2.41$, $\Delta = 2.6$, $\mathcal{J} = 0.75$. In this case, only 5% of the network occupies the first plateau, which has non-zero speed as the transition is approached. (d) Analogous plot to (b), showing the small amplitude, fast dynamics produced by crossing the H_{sup}.

XI. Conclusion

In this work we have studied the periodically driven Kuramoto model on random networks with a given degree distribution. A low-dimensional description was found, and a stability and partial bifurcation analysis developed, which allowed us to predict many of the states and transitions of the model for sufficiently weak coupling between nodes (see Sec.IX D). In particular we found a Takens-Bogdanov-Cusp (TBC) singularity, appearing for power-law degree distribution networks as the degree exponent was lowered, which separated branches of heterogeneous and

homogeneous network behavior. The unfolding of this singularity was used to uncover important dynamical transitions including: Saddle-Node-Infinite-Period, Hopf, and Limit-Point-of-Cycles (LPC), as well as multiple bistability regions that differed for the network types. Interestingly, we found that heterogeneous networks do not support bistability of driven synchronized states or bistability of quasi-periodic synchronized states and driven states (which is the case for homogeneous networks), but only bistability of large amplitude mutually synchronized and driven states. Moreover, we discovered that the LPC transition for the heterogeneous branch occurs with phase-slip dynamics for nodes with high degree and phase-trapped dynamics for nodes with low degree (on average), implying a new route to mutual synchronization for driven heterogeneous networks which allows for qualitatively different behavior depending on a node's degree. In addition, the structure of synchronization clusters for mutual and driven states was discussed and their transitions associated with bifurcations.

Still, we have yet to resolve all of the transitions associated with unstable cycles in the heterogeneous case (which could inform other interesting features of the dynamics), and the full unfolding of network bifurcations in the strong coupling region. Moreover, many real networks of interest have richer architecture than the simple degree heterogeneity discussed here: such as modular, fractal, and multi-scale structure [70, 87]. The effects of these features on network synchronization are interesting subjects for future work. Finally, the control of complex networks is of immense interest, both theoretical and practical. Our results can offer insight into the problem of controlling disordered oscillator networks and in particular the difficulty of building pacemakers for very heterogeneous networks that are driven away from their natural frequencies.

Part IV

COLLECTIVE WAVES IN DRIVEN RANDOMLY PINNED OSCILLATOR NETWORKS

Summary: In many coupled oscillator networks the local dynamics is not free, but can get stuck by quenched potentials and random forces. Often in such cases, the system requires a push supplied by external fields to excite its dynamics. However, most work in this area has assumed global coupling or simple lattice geometries in two and three dimensions. To our knowledge, this is the first extension of such behavior to complex networks. Though open questions remain, we find that heterogeneous topologies add the possibility of several new phenomena to this field, such as continuous depinning transitions from incoherent states to wave states in systems with non-elastic coupling [11] and the multistability of waves states.

XII. Introduction

The dynamics of large networks of coupled oscillators have been used to successfully capture the behavior of many systems in physics and biology [34, 78]. Much recent work in this area has focused on the synchronization of simple limit cycle oscillators in complex networks, which has demonstrated the importance of topology in effecting collective oscillations [34, 43, 72]. Often however, the behavior of coupled oscillators is complicated by local pinning forces and external fields, whose interplay can produce new phenomena, such as recurring waves and avalanches

[11] The continuity requires an infinite number of degree classes.

[72, 74–76]. These effects are seen in driven charge-density waves, disordered magnets systems, and networks of oscillating neurons and heart cells [74, 76, 80].

In this work, we explore the behavior of complex networks of nonlinear oscillators driven through quenched disorder with non-elastic coupling. Principally, we build a general framework for such dynamics on complex networks with large spectral gaps, and find new qualitative behavior such as the coexistence of multiple wave states and continuous depinning from incoherence for heterogeneous networks [76, 96].

XIII. Model and Mean-Field Dynamics

Let us consider a system where each degree of freedom is a pinned oscillator

$$\frac{d\theta}{dt} = E + \sin(\nu - \theta), \tag{54}$$

with a tendency to stick to a particular phase ν by a periodic potential, and can be driven to large oscillations with full phase slips if the driving, E, is sufficient to push the oscillator over the potential well (i.e., $E > 1$). In particular when the driving vanishes, the oscillator tends to a steady state, $\theta^* = \nu$. As E grows from 0 to 1, the steady state moves toward $\theta^* = \nu + \pi/2$, above which the oscillator never settles into an equilibrium and makes repeated revolutions around the circle. Eq.(54) describes the noiseless limit of a particle in a washboard and is the normal form for a SNIPER bifurcation (see Part III). Qualitatively, when $E \gtrsim 1$, Eq.(54) exhibits nonuniform, relaxation oscillations, as the oscillator slows down in the neighborhood of $\theta = \nu + \pi/2$.

Now, consider an interacting system of such oscillators, coupled in such a way as to favor the alignment of neighbors. We will focus on the simplest interaction that is odd under particle interchange, periodic in $(\theta_j - \theta_i)$, and that allows for phase slips, which is proportional to $\sin(\theta_j - \theta_i)$, but should be considered the first term in a general expansion with higher harmonics

[74–76]. Combining this interaction with Eq.(54) and with coupling constant J gives

$$\frac{d\theta_i}{dt} = E + \sin(\nu_i - \theta_i) + J\sum_j A_{ij}\sin(\theta_j - \theta_i), \tag{55}$$

that we will study in detail. Eq.(55) has the form of a Kuramoto-like system with local quenched potentials and a sharply peaked frequency distribution. Similar to synchronization, the system can be written in the suggestive form

$$\frac{d\theta_i}{dt} = E + \mathcal{I}m\left[e^{-i\phi_i}\left(J\sum_j A_{ij}e^{i\phi_j} + e^{i\nu_i}\right)\right], \tag{56}$$

from which we can define the complex order-parameter

$$z_i = \sum_j A_{ij}e^{i\phi_j}. \tag{57}$$

We are interested in the ensemble of such systems in the thermodynamic limit, where each member is assigned a set of ν's, chosen uniformly at random, with a fixed adjacency matrix, A_{ij}. We will assume that the system is self averaging, and therefore we can replace the order-parameter in a given realization by its ensemble average [73] [12]. The ensemble will be described by a distribution, $\rho(\vec{\theta}, t, \vec{\nu})$, that gives the probability density for the oscillators to be in state $\vec{\theta}$ at time t with pinnings $\vec{\nu}$, and which satisfies the continuity equation

$$\frac{\partial\rho}{\partial t} + \vec{\nabla}\cdot\left(\rho\frac{d\vec{\theta}}{dt}\right) = 0. \tag{58}$$

Given the distribution and the self-averaging assumption, the order-parameter is given by

$$z_i = \sum_j A_{ij}\int \rho e^{i\phi_j}\prod_{j\neq i} d\nu_j d\theta_j. \tag{59}$$

[12] This should be true if there are many copies of every position in the network, e.g. degrees in random networks.

By integrating Eq.(58) over θ_j and $\nu_j \; \forall \; j \neq i$, we are left with a similar equation for the marginal distribution $\rho_i(\theta_i, t, \nu_i)$

$$\frac{\partial \rho_i}{\partial t} + \frac{\partial}{\partial \theta_i}\left(\rho_i \frac{d\theta_i}{dt}\right) = 0, \tag{60}$$

and

$$z_i = \sum_j A_{ij} \int \rho_j e^{i\phi_j} d\nu_j d\theta_j. \tag{61}$$

As with synchronization, the marginal distribution can be decomposed into Fourier components with a power-series structure [55, 73]:

$$\rho_i(\theta_i, t, \nu_i) = \left(\frac{1}{2\pi}\right)^2 \left[1 + \sum_{n=1}^{\infty} \bar{a}_i^n(\nu, t) e^{in\theta_i} + \text{c.c.}\right], \tag{62}$$

where a_i satisfies

$$\frac{da_i}{dt} = iEa_i + \frac{1}{2}\left(e^{i\nu} + Jz_i\right) - \frac{1}{2}a_i^2\left(e^{-i\nu} + J\bar{z}_i\right), \tag{63}$$

and

$$z_i = \sum_j A_{ij} \int_0^{2\pi} a_j(\nu, t) \; \frac{d\nu}{2\pi}. \tag{64}$$

Eqs.(63) and (64) form the basis of the analysis below [72].

XIV. Static States

First, we will study states of Eq.(63) for which the system is static, both incoherent and coherent [74, 76]. Then, we will study how such states change stability and give rise to non-equilibrium wave states.

A. Incoherence

We saw above that each uncoupled oscillator can be pinned if $E < 1$, $(J = 0)$. When $J \neq 0$ and small, analogous solutions are possible that correspond to $z_i = 0$, which we call incoherent. In this case, each a_i tends to a steady state [13]

$$a_i^{ic} = e^{i\nu}\Big[iE + \sqrt{1 - E^2}\Big]. \tag{65}$$

To understand the stability of incoherence we look for the linear spectrum by adding perturbations, $a_i = a_i^{ic} + \eta(\nu, t)$ and $\bar{a}_i = \bar{a}_i^{ic} + \widetilde{\eta}(\nu, t)$, collecting terms to $\mathcal{O}(\eta)$, and looking for eigen-solutions, $\frac{d\eta}{dt} = \lambda\eta$ and $\frac{d\widetilde{\eta}}{dt} = \lambda\widetilde{\eta}$:

$$\begin{aligned}
\eta_i\big[\lambda + \sqrt{1 - E^2}\big] &= \frac{J}{2}\sum_j A_{ij}\left[\int_0^{2\pi}\left(\eta_j - (a_i^{ic})^2\widetilde{\eta}_j\right)\frac{d\nu}{2\pi}\right], \\
\widetilde{\eta}_i\big[\lambda + \sqrt{1 - E^2}\big] &= \frac{J}{2}\sum_j A_{ij}\left[\int_0^{2\pi}\left(\widetilde{\eta}_j - (\bar{a}_i^{ic})^2\eta_j\right)\frac{d\nu}{2\pi}\right].
\end{aligned} \tag{66}$$

We can find the discrete spectrum by integrating both sides of Eq.(66) [72]. This reduces the linear system to

$$v_i = \frac{J}{2\big[\lambda + \sqrt{1 - E^2}\big]}\sum_j A_{ij}v_j, \tag{67}$$

for some vector v_i, and has solutions:

$$\lambda^{ic} = \frac{J}{2}\mathcal{X} - \sqrt{1 - E^2}, \tag{68}$$

where $\mathcal{X}$'s are the eigenvalues of A. Furthermore, the spectrum has a continuous part when Eq.(66) is not surjective, which occurs for λ_{cont}^{ic} satisfying[75]:

[13] corresponding to $0 = E + \sin(\nu - \theta)$.

$$\lambda^{ic}_{cont} = -\sqrt{1 - E^2}. \tag{69}$$

For $E < 1$, we see that the continuous spectrum is negative, and the incoherent state is stable as long as $\lambda^{ic} < 0$. This suggests a loss of stability when

$$E^{DP} = \sqrt{1 - \left(\frac{J^{DP}\mathcal{X}^m}{2}\right)^2}, \tag{70}$$

where $\mathcal{X}^m$ is the largest eigenvalue of A, and DP refers to the typical name for this transition,"depinning" [74, 76]. Furthermore, the incoherent state disappears completely when the continuous spectrum approaches zero ($E \to 1$), which is consistent with the uncoupled results.

It is interesting to note that the coupling threshold, J^{DP}, vanishes as the largest eigenvalue of A diverges. An important class of networks for which this can occur is the annealed random graph, $A_{ij} = \frac{k_i k_j}{N\langle k\rangle}$, when the k's are distributed according to a power-law with some exponent. For this class, the maximum eigenvector is $v_i = k_i/\sqrt{N\langle k^2\rangle}$ with eigenvalue $\mathcal{X}^m = \langle k^2\rangle / \langle k\rangle$. The latter diverges for power-law distributions with exponents less than three and infinite cutoffs (Eq.(35)) [1, 2]. In the following we will study the behavior of such graphs in detail, though the results will be more general.

B. Coherence

Once the depinning transition is crossed, we expect an incoherent system to tend toward some coherent state, pulled by the interaction term in Eq.(55) that favors the phase alignment of neighbors. The simplest such states will be static with $z_i = const. \neq 0$, and will satisfy N

self-consistent relations for N unknowns

$$z_i^* = \sum_j A_{ij} \int_0^{2\pi} \frac{iE + \sqrt{|Jz_j^* + e^{i\nu}|^2 - E^2}}{J\bar{z}_j^* + e^{-i\nu}} \frac{d\nu}{2\pi}. \tag{71}$$

We further simplify the analysis by assuming that A is a non-negative matrix with a large spectral gap, such that it is well approximated by its positive, Perron-Frobenius eigenvectors, $A_{ij} \approx \mathcal{X}^m v_i^m u_j^m$, with eigenvalue $\mathcal{X}^m$ and right and left eigenvectors v_i^m and u_i^m, respectively [73, 79]. This reduces Eq.(71) to determining a single parameter, μ:

$$\begin{aligned}
\mu^* &= \sum_j u_j^m \int_0^{2\pi} a_j^* \frac{d\nu}{2\pi} \\
&= \sum_j u_j^m \int_0^{2\pi} \frac{iE + \sqrt{|J\mathcal{X}^m v_j^m \mu^* + e^{i\nu}|^2 - E^2}}{J\mathcal{X}^m v_j^m \bar{\mu}^* + e^{-i\nu}} \frac{d\nu}{2\pi}.
\end{aligned} \tag{72}$$

In practice, we find that μ^* has solutions with rotational symmetry, $\mu^* = R^* e^{i\Psi_0}$ for any Ψ_0.

For these coherent static states, we can determine the spectrum as above, which gives the linear system:

$$\begin{aligned}
\eta_i\big[\lambda - q_i\big] &= \frac{J\mathcal{X}^m v_i^m}{2}\left[C - (a_i^*)^2 \widetilde{C}\right] \\
\widetilde{\eta}_i\big[\lambda - q_i\big] &= \frac{J\mathcal{X}^m v_i^m}{2}\left[\widetilde{C} - (\bar{a}_i^*)^2 C\right] \\
C &= \sum_j u_j^m \int_0^{2\pi} \eta_j \frac{d\nu}{2\pi} \\
\widetilde{C} &= \sum_j u_j^m \int_0^{2\pi} \widetilde{\eta}_j \frac{d\nu}{2\pi}
\end{aligned} \tag{73}$$

$$q_i \equiv -\sqrt{|J\mathcal{X}^m v_j^m \mu^* + e^{i\nu}|^2 - E^2} \tag{74}$$

The discrete part of the spectrum can be found by solving for the η's in the top two relations of (73), multiplying by u_j^m, summing over j, integrating over ν, and eliminating the constants

C and $\widetilde{C}$ [72]. This produces a condition for the discrete spectrum λ^c:

$$\left| \frac{\sum_j u_j^m \int_0^{2\pi} \frac{J\mathcal{X}^m v_j^m (a_j^*)^2}{2[\lambda^c - q_j]} \frac{d\nu}{2\pi}}{\sum_j u_j^m \int_0^{2\pi} \frac{J\mathcal{X}^m v_j^m}{2[\lambda^c - q_j]} \frac{d\nu}{2\pi} - 1} \right|^2 = 1. \tag{75}$$

which in general has two real solutions: zero and non-zero. The former is a consequence of the rotational symmetry for these states. On the other hand, the continuous spectrum is given by:

$$\lambda^c_{cont} = q_i(\nu). \tag{76}$$

corresponding to a perturbation of the ith oscillator with pinning ν.

1. Zero Drive

It is instructive to consider transitions in the zero-drive limit, which is the first step in determining the possible dynamics for this system and will help us to understand the influence of network topology. Importantly, we find that many of the behaviors that emerge in this limit carry over to non-zero drives.

When E=0 there are two competing tendencies: disorder from the random pinnings and coherence from the coupling. We find that these tendencies produce various static coherent states that can coexist with each other and the incoherent state, and generates a transition type in addition to depinning. The former occurs when the eigenvalue of a coherent state associated with rotational symmetry is degenerate, and is thus a sort of Takens-Bogdanov, TB, bifurcation (see Sec.IX D). This point prefaces the appearance of stable and unstable coherent states with rotational symmetry. Once produced, the unstable state can collide with the incoherent state, resulting in the depinning transition of Eq.(70), or collide with other stable coherent states resulting in further TB transitions, which are shown in Fig.13. Unlike the complete graph case where only one TB occurs (beneath the depinning transition), *many* TB transitions occur for

heterogeneous networks, which implies new phenomena [74, 76].

To find the locations of TB bifurcations, we note that as the bifurcation is approached, the two eigenvalues of a coherent state's discrete spectrum meet at zero, which suggests expanding Eq.(75) in powers of λ^c, and enforcing that terms of order λ^c vanish. This gives the criterion:

$$Re\Bigg[\left(\sum_j u_j^m \int_0^{2\pi} \frac{\mathcal{X}^m v_j^m (a_j^*)^2}{q_j^2}\frac{d\nu}{2\pi}\right)\left(\sum_j u_j^m \int_0^{2\pi} \frac{\mathcal{X}^m v_j^m (\bar{a}_j^*)^2}{\bar{q}_j}\frac{d\nu}{2\pi}\right) - \left(\sum_j u_j^m \int_0^{2\pi} \frac{\mathcal{X}^m v_j^m}{q_j^2}\frac{d\nu}{2\pi}\right)\left(\sum_j u_j^m \int_0^{2\pi} \frac{\mathcal{X}^m v_j^m}{\bar{q}_j}\frac{d\nu}{2\pi} - \frac{2}{J}\right)\Bigg] = 0. \quad (77)$$

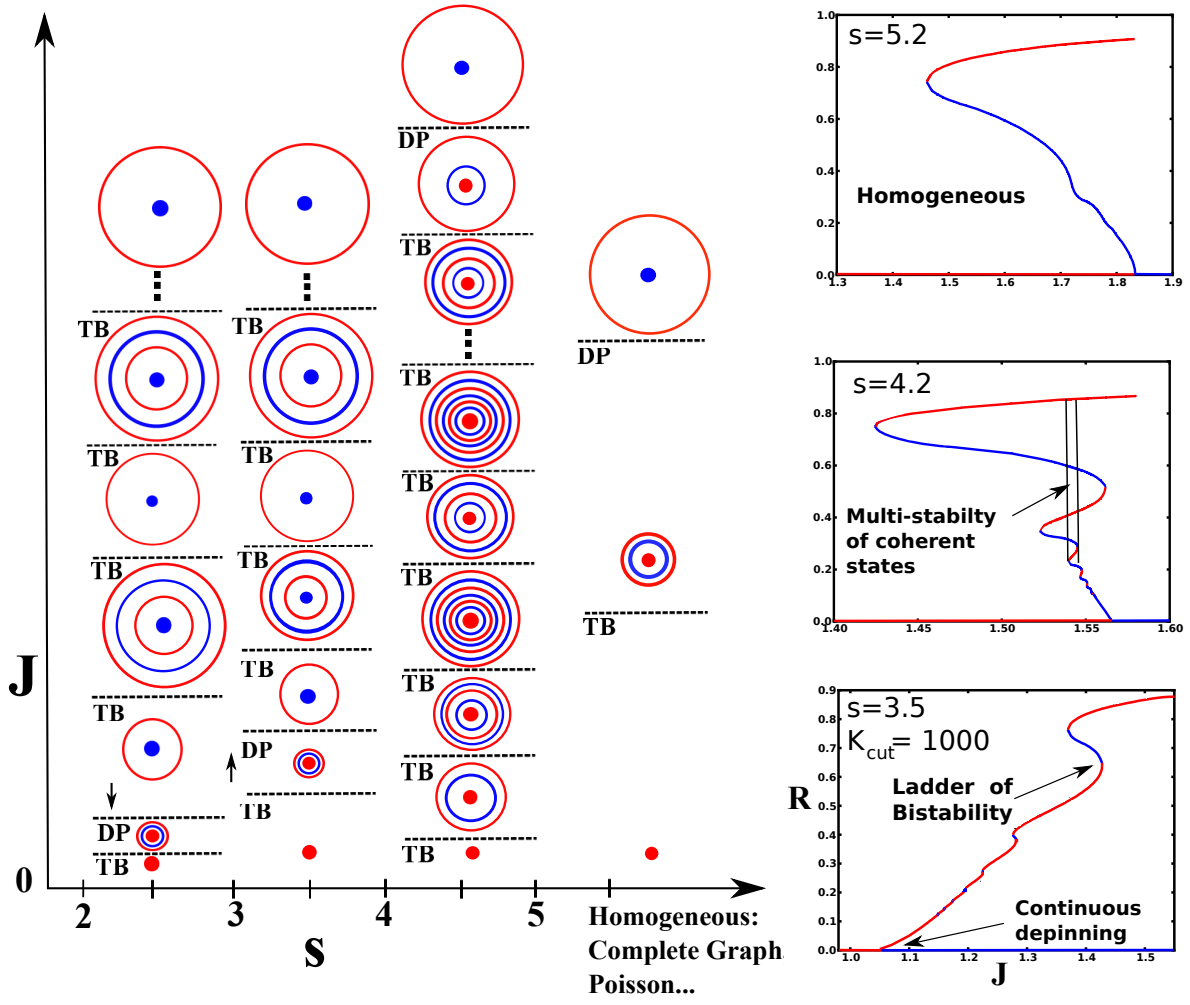

Figure 13: Schematic diagram of states and transitions in the zero-drive limit for random networks with power-law distributions shown as a function of the distribution exponent, s, and the coupling J. Stable states are shown in red and unstable in blue. The transitions are labeled, TB, for Takens-Bogdanov and DP for depinning. Arrows indicate the direction that transitions move when the degree Cut-off, K_{cut} goes to infinity (see Eq.(35)). Bifurcation diagrams of the coherence R versus J are shown to the right.

A diagram showing the possible states and transitions for un-driven random networks is illustrated in Fig.13. In particular, we find that for homogeneous networks such as the complete graph, Poisson distributed, or power-law distributed networks (Eq.(35)) with exponents (s), $s \gtrsim 5$, there is only one TB transition, and it occurs for couplings below the depinning point. In this region, stable coherent states take a form in which nodes that have pinning phases equal to and π displaced from the mean-field, have steady states equal to the mean-field. For other pinnings, phases follow a sinusoidal pattern with an amplitude that decreases with degree. An example is shown in Fig.14(a).

On the other hand, as the exponent is lowered many additional TB transitions occur, above and below the depinning transition depending on the value of s. These signal the emergence of interesting stable coherent states in which we find qualitatively different patterns for low and high degree nodes [72]. For example, stable states can emerge where $k = 1, 2, ...k_{top}$ nodes have equilibrium phases that are reminiscent of the pinned state (i.e., oscillators stay very near their pinning phases). In particular, steady state phases with pinnings that are π displaced from the mean-field are not equal to the mean-field, but remain π displaced[14]. However, nodes with degree greater than k_{top} have the sinusoidal coherence behavior described above. Examples are shown in Fig.14(b-c). Also, it is very interesting that many such states can be simultaneously stable, as illustrated in Fig.13 and Fig.14, implying that stable coherent states are not unique for heterogeneous networks (including "ladders" of bistability for networks with degree exponent $s \lesssim 5$ – see Figs. 13 and 17).

It should be noted that the boundaries between regions for random power-law networks in Fig.13 are not sharply divided by integer values of s in general (similar to Part III). Only the DP transition, and any others whose properties are dependent on it, will be functions of the adjacency matrix alone, and therefore, on moments of the degree distribution. If certain

[14] In fact, we find that it is the switching of certain nodes with $\nu = \Psi_0 + \pi$ from $\theta^* = \nu$ to $\theta^* = \Psi_0$ that is the signature of discontinuous jumps among stable states, and is a new behavior not seen in homogeneous networks.

moments grow to infinity, such as the second, the DP transition goes to zero, and pushes the TB beneath it to zero (see Fig.13). As mentioned, this can occur for power-law networks with degree exponents $s < 3$ and infinite support. Moreover, we find that the distance between the DP and the TB beneath it, also goes to zero for exponents $s \lesssim 4$ with large K_{cut}, even though the DP can occur for finite J. This finding has important implications for the nature of the DP transition with drive for such networks. However, it remains for future work to describe the complete set of TB transitions as a function of s (typically we find only weak dependence on K_{cut}, for large values of K_{cut}).

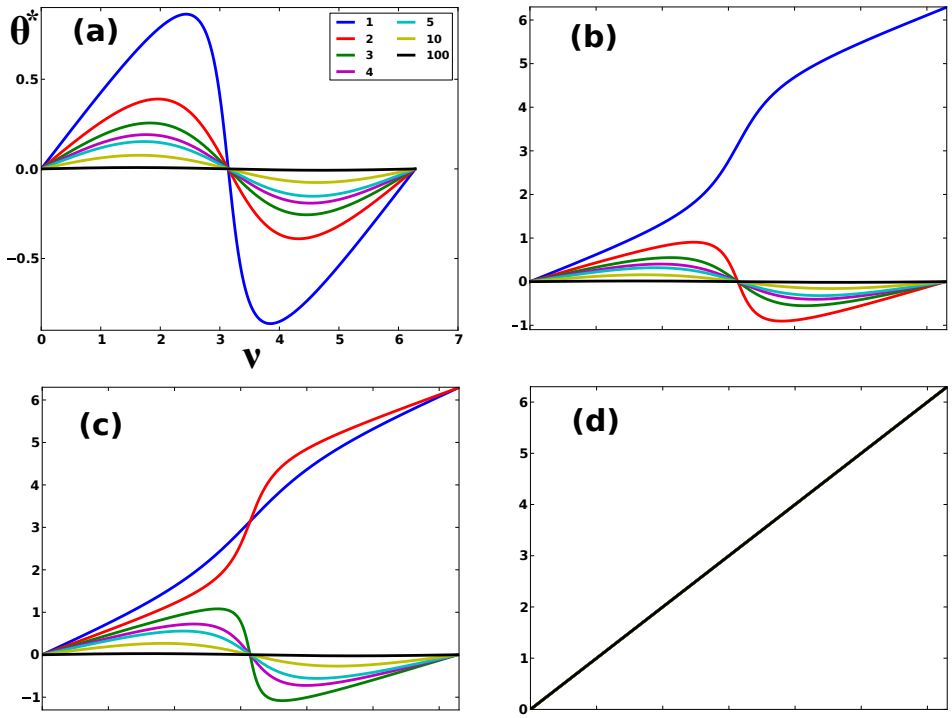

Figure 14: Multiple stable steady-state phase distributions for a power-law network with parameters $s = 4.2$, $K_{cut} = 10000$, $J = 1.541$ and $E = 0$, shown versus pinning, ν. Different colors represent various degree classes, with a legend given in (a). The subfigures (a-d) are ordered according to decreasing coherence, with (d) showing the pinned state, $R = 0$.

2. Non-Zero Drive

For non-zero drives, we find an additional type of transition for coherent static states, when the continuous spectrum touches the origin. This means that some group of oscillators can no

longer remain stationary, and begin making full revolutions around the circle. For example, for random networks with couplings just below the depinning transition, the system has an unstable coherent state that branches off from the incoherent state [74]. If the system is in the former, we find that nodes with the maximum degree and with pinnings $\nu_{k_{max}} = \Psi + \pi$, can begin to wind if the coupling is lowered enough, and destroy the equilibrium when:

$$0 = q_{k_{max}}(\pi) = \sqrt{(Jk_{max}R)^2 - E^2}, \tag{78}$$

or

$$1 - E = Jk_{max}R. \tag{79}$$

In particular if the maximum degree is very large, this implies that the DP transition is not only associated with a collective instability of all oscillators around their pinnings, but a local instability as well, in very high degree nodes for networks without compact support.

XV. Wave States

In addition to static states discussed, there are wave states when $E \neq 0$, for which we find $\mu = Re^{iVt}$, where the magnitude of the system's coherence, R, tends to a constant, while its average phase rotates at a non-zero, constant velocity [74–76]. We find that such states are limiting solutions when the coupling and drive are large, for which the oscillator tendencies to cohere with neighbors and move with the driving are cooperative. Importantly, we find that transitions for wave states are very similar to the zero-drive results above.

We can get a sense for what behavior underlies wave states by substituting the order-parameter ansatz into Eq.(63), and peeling off the constant velocity piece, $a_i(t, \mu) = e^{iVt}b_i(t, \mu)$,

where $b_i(t,\mu)$ satisfies:

$$\frac{db_i}{dt} = i(E-V)b_i + \frac{1}{2}\left(e^{i(\nu-Vt)} + J\mathcal{X}^m v_i^m R\right) - \frac{1}{2}b_i^2\left(e^{-i(\nu-Vt)} + J\mathcal{X}^m v_i^m R\right), \tag{80}$$

This form suggests that we should look for solutions in a co-moving frame, $\zeta = \nu - Vt$, so that b_i satisfies a time-autonomous evolution. For such solutions, every oscillator with the same graph position, i, undergoes the same dynamics but shifted in time depending on its pinning,

$$-V\frac{db_i}{d\zeta} = i(E-V)b_i + \frac{1}{2}\left(e^{i\zeta} + J\mathcal{X}^m v_i^m R\right) - \frac{1}{2}b_i^2\left(e^{-i\zeta} + J\mathcal{X}^m v_i^m R\right), \tag{81}$$

and

$$R = \sum_j u_j^m \int_0^{2\pi} b_j(\zeta,t)\,\frac{d\zeta}{2\pi}. \tag{82}$$

The b-functions, and constants R and V are difficult to determine in general without resorting to integrating Eq.(81); however, we can find their limiting forms when the coupling is large, $J = 1/\epsilon \gg 1$, for which we expect to have wave solutions as long as $E \neq 0$. In this limit we assume that:

$$b_i(\zeta) = b_{i,0} + b_{i,1}\epsilon + b_{i,2}\epsilon^2 + ... \tag{83}$$

$$R = R_0 + R_1\epsilon + R_2\epsilon^2 + ... \tag{84}$$

$$V = V_0 + V_1\epsilon + V_2\epsilon^2 + ..., \tag{85}$$

and can find the coefficients by substituting the expansions into Eq.(81), and collecting terms to a given order [74]. This determines b to that order as a function of R and V. Next, R and

V are determined by substituting b into Eq.(82), and computing the integral's real part, which gives R to the same order as b, and the imaginary part, which gives V to the previous order, when the imaginary part is set to zero. Following this program, we find:

$$b_i(\zeta) = 1 + \frac{i \sin\zeta}{J\mathcal{X}^m v_i^m \sum_j u_j^m} + \frac{iE\cos\zeta - \frac{i}{2}\sin 2\zeta - \frac{1}{2}\sin^2(\zeta)}{\left(J\mathcal{X}^m v_i^m \sum_j u_j^m\right)^2} + ... \tag{86}$$

$$R = \sum_j u_j^m - \frac{\sum_j u_j^m/(v_j^m)^2}{\left(2J\mathcal{X}^m \sum_j u_j^m\right)^2} + ... \tag{87}$$

$$V = E\left[1 - \frac{\sum_j u_j^m/(v_j^m)^3}{2\left(J\mathcal{X}^m \sum_j u_j^m\right)^2 \sum_j u_j^m/v_j^m}\right], \tag{88}$$

showing that in the limit of large coupling, each oscillator has an average velocity that is proportional to the driving field. Moreover, the relative positions of each oscillator are modulated by the same waveform in ν, whose amplitude is a decreasing function of each oscillator's eigenvector component. This implies that graph positions with large components rotate with nearly perfect coherence, while those with small components rotate with greater dispersion. Example trajectories are shown for random networks in Fig.15-(a) that demonstrate this behavior.

XVI. Stability Patterns

Now that we have discussed the major transitions and states in certain limiting cases, the central questions remaining are: how are the limiting descriptions connected through transitions and how does the picture depend on network properties. First, we can gain traction on this front by looking at the behavior of homogeneous networks. In this part of parameter space, we find stability diagrams such as Fig.16, which is known for the complete graph [74]. For example, if we imagine decreasing the coupling from the depinning transition, while keeping

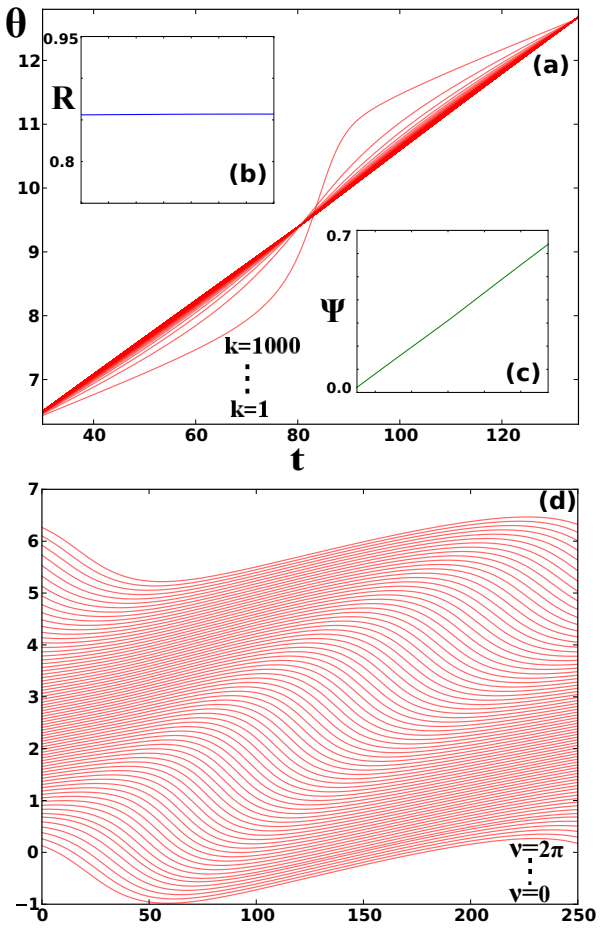

Figure 15: Example trajectories of a wave state versus time for a discretized version of Eq.(63) on an annealed random network with power-law distribution and $s = 3.5$, $K_{cut} = 1000$, $E = 0.1$, and 75 pinnings distributed evenly. (a) phases for different degree classes, with pinning $\nu = 0$ and $J = 1.45$. (b) magnitude of the order-parameter. (c) phase of the order-parameter. (d) phases for different pinnings and degree, $k = 1$ with $J = 1.30$, showing a wave state where the degree-one nodes fail to make full phase-slips, and are therefore passed by the mean-field and higher degree nodes.

the drive fixed, we find the stable pinned state, a stable wave state of the form described in Eq.(81), and an unstable coherent static state with small coherence level. As J is decreased further, the coherence of the unstable state increases until Eq.(79) occurs, and an unstable wave is formed. Continuing this process, we find that the size of the unstable wave increases until it is coincident with the stable wave, at which point both are annihilated in a Limit-Point-of-Cycles, LPC, transition. The order-parameters, R and V, are discontinuous over the latter transition.

Though the picture is more complicated for heterogeneous networks, because of the possibility of having multiple coherent states stable simultaneously (Figs.13-14), we expect that

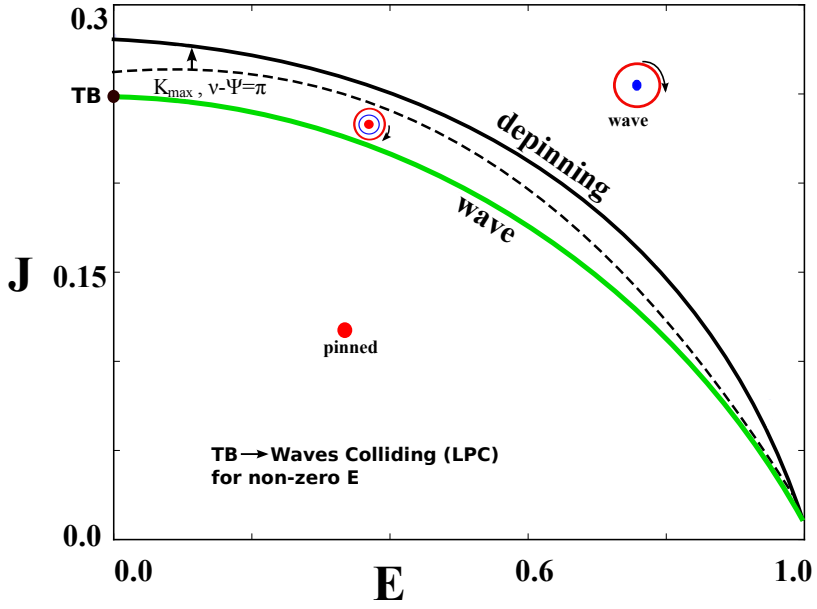

Figure 16: Stability diagram for a Poisson distributed annealed random network with average degree 5.6 and 15000 nodes. The depinning transition is shown in black, the transition of Eq.(79) is shown as a dashed line, and the *LPC*-wave transition is shown in green. Stable and unstable states are illustrated in red and blue, respectively.

as for homogeneous networks, TB bifurcations without drive, turn into LPC transitions with drive (see Fig.17). If true, this means that the DP transition to a wave state should be continuous in cases where the zero-drive TB and DP are coincident (i.e., $s \lesssim 4$), as mentioned in Sec.XIV B 2[15]. Also, we expect that unstable waves can appear from static states through transitions such as the one described by Eq.(79). However, constructing full stability diagrams for power-law networks with exponents $2 \lesssim s \lesssim 5$ has been more difficult, because such networks require including very many degree classes in simulations and tend to have larger fluctuations for finite N. As a consequence, the full picture remains for future work.

Nevertheless, we do observe qualitatively new behavior as prefaced in the zero-drive limit. For example, Fig.17 shows the average magnitude of the order parameter verus J for simulations on a network with $s = 3.5$ and $E = 0.1$, compared to the un-driven results. We can see that each driven point roughly corresponds to a point on the un-driven curve[16].

[15] It is rigorously true that the depinning transition is continuous for $s < 3$; it remains to be demonstrated analytically that this occurs for the more general $s < 4$.

[16] The fact that the driven curve does not go to zero, we believe, is due to the finite number of pinning points

For the un-driven network in Fig.17, we find that every stable branch has a different number of degree classes whose nodes stay near their pinning phases, and in particular, nodes with $\nu = \pi + \Psi_0$, have phases $\theta^* = \nu$: in the top branch there are zero such nodes, in the second branch there are degree-one nodes, in the third branch there are degree-one and degree-two nodes, etc. Interestingly for this graph exponent, we can see that there is a "ladder" of bistability regions, where each branch can be bistable with the one beneath it. Correspondingly, for the driven network we find that each branch specifies which degree classes have zero average velocity, and simply oscillate around their pinnings (phase-trapped motion) with all other classes having average velocity equal to the mean-field (see Fig.15-B). This means that the bistability regions that connect neighboring branches in the zero-drive limit, correspond to bistability of wave states for non-zero drive with different numbers of degree classes that have phase-trapped motion. Moreover, Fig.17 shows that the DP transition is approximately continuous, as mentioned. For couplings very near J^{DP}, only the highest degree nodes can be depinned.

In the future, it will be determined how these results are extended to $E \lesssim 1$.

XVII. Conclusion

In this work we have analyzed the dynamics of complex networks of nonlinear oscillators that are driven through quenched disorder and found new dynamical behaviors, including new states and transitions for heterogeneous networks. In the near future we will extend the weakly driven results, uncover the full stability diagrams, and connect the behaviors with changes in the degree exponent. Also, we will explore more general networks, including modular systems, where the large spectral gap approximation should break down. We expect to build a more general approach for such networks, by expanding the adjacency matrix into graph modes which are close to the Frobenius. Extensions in this direction could be used to study such

used in simulations.

real phenomena as neuronal avalanches [80]. Furthermore, we will explore the effects of general pinning potentials and random fields, which are relevant in many applications, including charge-density waves.

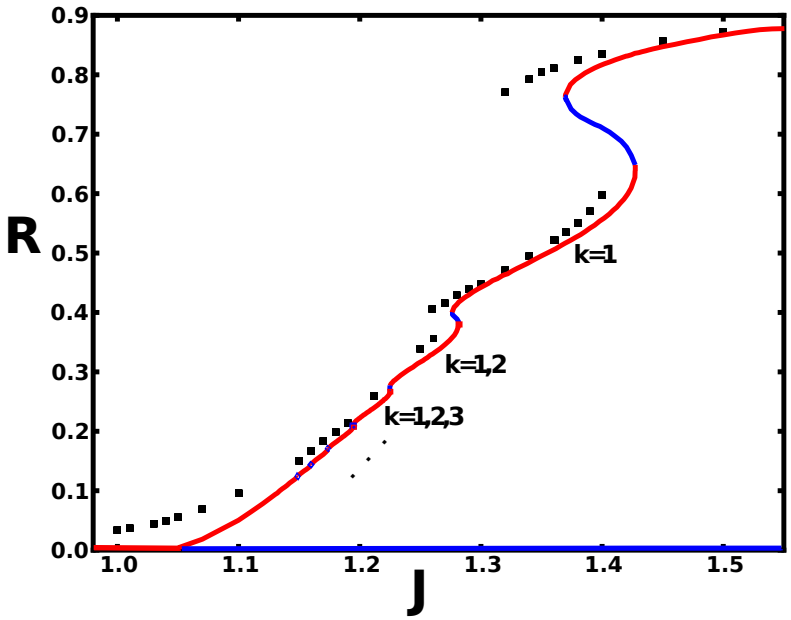

Figure 17: Average magnitude of the order parameter (black) versus the coupling strength for a random network with a power-law distribution: $s = 3.5$, $K_{cut} = 1000$, and $E = 0.1$. Stable and unstable branches for the zero-drive case are shown for comparison in red and blue, respectively. Each branch is labeled with the degree classes that have zero average velocity for the driven case (phase-trapped motion), and with the degree classes that remain near their pinnings (e.g., $\theta^*(\nu = \pi + \Psi_0) = \nu$) for the un-driven case.

Part V

FINAL CONCLUSIONS AND PROSPECTS

This dissertation has addressed several important problems in non-equilibrium pattern formation and nonlinear dynamics mediated through complex networks. Analytical calculations and numerical methods allowed us to compute velocities and profiles of epidemic fronts on interconnected networks, and various nonlinear transitions associated with collective waves and oscillations in coupled oscillator networks. New quantitative techniques were developed and new qualitative behavior was discovered, both of which provided insights into the effects of topology (especially local heterogeneity and correlations) on several general dynamical processes. In particular this work has demonstrated new behavior on complex networks whose nonlinear dynamics is excited by external drive.

Beyond the specific conclusions and projections offered at the end of Parts II-IV, we mention a few related areas that are candidates for future work. The first concerns the application of network theory to swarm behavior, which is central to many phenomena such as schooling fish, flocking birds, and colonizing bacteria [82]. Although this is an active field of research, most theoretical studies have assumed geometric or global interaction structure, even though it is well known that social animals interact through various complex networks [93–95]. Our previous work suggests that the addition of network features such as heterogeneity and hierarchy should produce a variety of new spatiotemporal patterns, which can be analyzed using some of the techniques that we have developed above. Also, this research could have important applications in fields such as robotics, where there is much interest in developing autonomous mobile sensor networks to perform complex tasks by mimicking swarming behavior.

The second area for future work concerns network corse-graining and renormalization, which

could give insight into a more general understanding of critical phenomena occurring on complex networks. Are there specific relevant topological features that drive certain types of criticality, and if so how do we find them? Much focus is given to local properties of networks, but as we know from the theory of critical phenomena, universal properties of continuous phase transitions typically depend on structures and symmetries after coarse-graining. Not only are critical phenomena central to many important applications, but such work could demonstrate a more general way to conceptualize continuous phase transitions in statistical physics.

[1] M. E. J. Newman, S. H. Strogatz, and D. J. Watts, Phys. Rev. E **64**, 026118 (2001).

[2] M. E. J. Newman, *Networks: An Introduction* (Oxford University Press, 2010).

[3] A. Barrat, M. Barthélemy, and A. Vespignani, *Dynamical Processes on Complex Networks* (Cambridge University Press, 2008).

[4] M. E. J. Newman, Phys. Rev. E **67**, 026126 (2003).

[5] M. E. J. Newman, Phys. Rev. E **66**, 016128 (2002).

[6] E. Kenah and J. M. Robins, Phys. Rev. E **76**, 036113 (2007).

[7] H.S. Wilf, *Generatingfunctionology, second ed.* (Academic Press, London, 1994).

[8] A. Vazquez, Phys. Rev. E **74**, 066114 (2006).

[9] A. Allard, P.-A. Noël, L. J. Dubé, and B. Pourbohloul, Phys. Rev. E **79**, 036113 (2009).

[10] P.-A. Noël, B. Davoudi, R. C. Brunham, L. J. Dubé, and B. Pourbohloul, Phys. Rev. E **79**, 026101 (2009).

[11] P.-A. Noël, A. Allard, L. Hébert-Dufresne, V. Marceau, and L. J. Dubé, Phys. Rev. E **85**, 031118 (2012).

[12] This is very general. For instance, one could specify as many types as there are nodes in the network, from which virtually any network could be constructed.

[13] E. Volz, J. Math. Biol. **56**, 293 (2008).

[14] J. C. Miller, J. Math. Biol. **62**, 349 (2011).

[15] J. C. Miller, A. C Slim, and E. M. Volz, J.R. Soc. Interface **9**, 890 (2011).

[16] J. P. Gleeson, S. Melnik, J. A. Ward, M. A. Porter, and P. J. Mucha, Phys. Rev. E **85**, 026106 (2012).

[17] N. Goldenfeld, *Lectures on Phase Transitions and the Renormalization Group* (Westview Press, 1992).

[18] I. Hanski, Nature **396**, 41 (1998).

[19] M. J. Keeling and P. Rohani, *Modeling Infectious Diseases in Humans and Animals* (Princeton University Press, 2007).

[20] I. Sazonov, M. Kelbert, and M. Gravenor, Math. Model. Nat. Phenom. **3**, 28 (2008).

[21] E. Brunet and B. Derrida, Phys. Rev. E **56**, 2597 (1997).

[22] W. Saarloos, Phys. Rep. **386**, 29 (2003).

[23] D. Panja, Phys. Rep. **393**, 87 (2004).

[24] S. Theodorakis and E. Leontidis, Phys. Rev. E **65**, 026122 (2002).

[25] M. Dickison, S. Havlin, and H.E. Stanley, Phys. Rev. E **85**, 066109 (2012).

[26] B. Karrer and M. E. J. Newman, Phys. Rev. E **82**, 066118 (2010).

[27] A. Saumell-Mendiola, M. A. Serrano, and M. Boguñá, Phys. Rev. E **86**, 026106 (2012).

[28] D. T. Gillespie and L. R. Petzold, J. Chem. Phys. **119**, 8229 (2003).

[29] M. A. Gibson and J. Bruck, J. Phys. Chem. A **104**, 1876 (2000).

[30] V. Belik, T. Geisel, and D. Brockmann, Phys. Rev. X **1**, 011001 (2011).

[31] F. Simini, M. C. González, A. Maritan, and A. L. Barabási, Nature **484**, 96 (2012).

[32] N. Perra, A. Baronchelli, D. Mocanu, B. Goncalves, R. Pastor-Satorras, and A. Vespignani, Phys. Rev. Lett. **109**, 238701 (2012).

[33] C.D. Meyer, *Matrix Analysis and Applied Linear Algebra* (SIAM, 2001).

[34] J. A. Acebrón, L. L. Bonilla, C. J. P. Vicente, F. Ritort, and R. Spigler, Rev. Mod. Phys. **77**, 137 (2005).

[35] A. Balanov, N. Janson, D. Postnov, and O. Sosnovtseva, *Synchronization: From Simple to Complex* (Springer, Berlin, 2009).

[36] S. Strogatz, Physica D **143**, 1 (2000).

[37] Y. Kuramoto, *Chemical Oscillations, Waves, and Turbulence* (Springer, Berlin, 1984).

[38] H. Sompolinsky, D. Golomb, and D. Kleinfeld, Proc. Natl. Acad. Sci. **87**, 7200 (1990).

[39] I. Z. Kiss, Y. Zhai, and J. L. Hudson, Science **296**, 1676 (2002).

[40] J. Pantaleone, Phys. Rev. D **58**, 073002 (1998).

[41] K. Wiesenfeld, P. Colet, and S. H. Strogatz, Phys. Rev. E **57**, 1563 (1998).

[42] S. N. Dorogovtsev, A. V. Goltsev, and J. F. F. Mendes, Rev. Mod. Phys. **80**, 1275 (2008).

[43] A. Arenas, A. Diaz-Guilera, J. Kurths, Y. Moreno, and C. Zhou, Phys. Rep. **469**, 93 (2008).

[44] A. Barrat, M. Barthélemy, and A. Vespignani, *Dynamical Processes on Complex Networks* (Cambridge University Press, 2008).

[45] J. Gómez-Gardeñes, S. Gómez, A. Arenas, and Y. Moreno, Phys. Rev. Lett. **106**, 128701 (2011).

[46] P. S. Skardal and A. Arenas, Phys. Rev. E **89**, 062811 (2014).

[47] P. S. Skardal, J. Sun, D. Taylor, and J.G. Restrepo, Europhys. Lett. **101**, 20001 (2013).

[48] J. C. Dunlap, J.J. Loros, and P.J. Decoursey, *Chronobiology: Biological Timekeeping* (Sinauer Associates, 2003).

[49] Y.-Y. Liu, J.-J. Slotine, and A.-L. Barabási, Nature **473**, 167 (2011).

[50] C. Liu, D.R. Weaver, S.H. Strogatz, and S.M. Reppert, Cell **91**, 855 (1997).

[51] H. Sakaguchi, Prog. Theor. Phys., **79**, 39, (1988).

[52] T. M. Antonsen, R. T. Faghih, M. Girvan, E. Ott, and J. Platig, Chaos **18**, 037112 (2008).

[53] L. M. Childs and S. H. Strogatz, Chaos **18**, 043128 (2008).

[54] J. Um, H. Hong, and H. Park, Phys. Rev. E **89**, 012810 (2014).

[55] E. Ott and T. M. Antonsen, Chaos **18**, 037113 (2008).

[56] Y. Wang and F. J. Doyle, Automatica, **47**(6), 1236 (2011).

[57] D. Pazó and E. Montbrió, Phys. Rev. X 4, 011009 (2014).

[58] P. Ji, T. K. D. M. Peron, F. A. Rodrigues, and J. Kurths, Scientific Reports **4**, 4783 (2014).

[59] J. D. Crawford, Rev. Mod. Phys. **57**, 991 (1991).

[60] S. Strogatz, *Nonlinear Dynamics and Chaos* (Westview Press, 2001).

[61] YU. A. Kuznetsov, *Elements of Applied Bifurcation Theory, Third Edition* (Springer, Berlin, 2004).

[62] YU. A. Kuznetsov, SIAM J. Numer. Anal. **36**, 1104 (1999).

[63] YU. A. Kuznetsov, Int. J. Bifurcation Chaos **15**, 3535 (2005).

[64] G. Danglemayr and J. Guckenheimer, Arch. Rat. Mech. Anal. **97**, 321 (1987).

[65] J. Guckenheimer and I. S. Labouriau, Bull. Math. Bio. **55**, 937 (1993).

[66] R. Mohieddine, *Chaos in the Hodgkin-Huxley Equations: The Takens-Bodganov Cusp Bifurcation* (Cornell University Mathematics Department Senior Thesis, 2008).

[67] M. H. Jensen, P. Bak, T. Bohr, Phys. Rev. Lett. **50**, 1637 (1983).

[68] J. R. Engelbrecht and R. Mirollo, Phys. Rev. Lett. **109**, 034103 (2012).

[69] C. Song, S. Havlin, and H. A. Makse, Nature **433**, 392 (2005).

[70] J. Hindes, S. Singh, C. R. Myers, and D. J. Schneider, Phys. Rev. E **88**, 012809 (2013).

[71] The annealed approximation for configuration model networks is less quantitatively accurate for networks with small average neighbor-degrees (such as the Poisson distributed network shown in

Fig.10 (b)). This has made it difficult to verify bistability unambiguously for these networks, because the region of parameter space where it is predicted to exist is small (Sec.X A).

[72] J. Hindes and C. R. Myers, Chaos **25**, 073119 (2015).

[73] G. Barlev, T. M. Antonsen, and E. Ott, Chaos **21**, 025103 (2011).

[74] S. H. Strogatz, C. M. Marcus, R. M. Westervelt, and R. E. Mirollo, Physica D **36**, 23 (1989).

[75] S. Strogatz, C. M. Marcus, R. M. Westervelt, and R. E. Mirollo, Phys. Rev. Lett. **61**, 2380 (1988).

[76] K. Saunders, J. M. Schwarz, M. C. Marchetti, and A. Middleton, Phys. Rev. B **70**, 024205 (2004).

[77] S. H. Strogatz and R. E. Mirollo, J. Statist. Phys. **63**, 3 (1991).

[78] Y. Tang, F. Qian, H. Gao, and J. Kurths, Annual Reviews in Control **38**, 184 (2014).

[79] R. R. Nadakuditi and M. E. J. Newman, Phys. Rev. E **87**, 012803 (2013).

[80] E. J. Friedman and A. S. Landsberg, Chaos **23**, 013135 (2013).

[81] P. W. Anderson, Science, New Series, **177** (4047), 393 (1972).

[82] T. Vicsek and A. Zafeiris, Phys. Rep., **517** (3-4), 71 (2012).

[83] James Sethna, *Statistical Mechanics: Entropy, Order Parameters, and Complexity* (Oxford University Press, 2006).

[84] D. J. Watts and S. H. Strogatz, Nature **393**, 440 (1998).

[85] R. Albert and A. L. Barabási, Rev. Mod. Phys. **74**, 47 (2002).

[86] A. L. Barabási and R. Albert, Science **286**, (5439) 509 (1999).

[87] C. Song, S. Havlin, and H. A. Makse, Nature **433**, 392 (2005).

[88] M. Kivelä, A. Arenas, M. Barthelemy, J. P. Gleeson, Y. Moreno, and M. A. Porter, Journ. Comp. Netw. **2**, (3) 203 (2014).

[89] L. M. Pecora and T. L. Carroll, Phys. Rev. Lett. **80**, 2109 (1998).

[90] L. Kocarev and P. Amato, Chaos **15**, 024101 (2005).

[91] B. C. Coutinho, A. V. Goltsev, S. N. Dorogovtsev, and J. F. F. Mendes, Phys. Rev. E **87**, 032106 (2013).

[92] D. T. Citron and C. R. Myers, APS March Meeting 2015, Vol. 60, Num.1, T48.00002.

[93] L. Mier-y-Teran-Romero, E. Forgoston, I. B. Schwartz, IEEE Trans Robot. **28**, 1034 (2012).

[94] M. Nagy, Z. Akós, D. Biro, and T. Vicsek, Nature **464**, 08891 (2010).

[95] M. Aldana, V. Dossetti, C. Huepe, V. M. Kenkre, and H. Larralde, Phys. Rev. Letts. **98**, 095702

(2007).

[96] A. A. Middleton, Phys. Rev. Letts. **68**, 670 (1992).